National Library of Canada
Bibliothèque nationale du Canada

Canadian Theses Service
Service des thèses canadiennes

Ottawa, Canada
K1A 0N4

NOTICE

The quality of this microform is heavily dependent upon the quality of the original thesis submitted for microfilming. Every effort has been made to ensure the highest quality of reproduction possible.

If pages are missing, contact the university which granted the degree.

Some pages may have indistinct print especially if the original pages were typed with a poor typewriter ribbon or if the university sent us an inferior photocopy.

Reproduction in full or in part of this microform is governed by the Canadian Copyright Act, R.S.C. 1970, c. C-30, and subsequent amendments.

AVIS

La qualité de cette microforme dépend grandement de la qualité de la thèse soumise au microfilmage. Nous avons tout fait pour assurer une qualité supérieure de reproduction.

S'il manque des pages, veuillez communiquer avec l'université qui a conféré le grade.

La qualité d'impression de certaines pages peut laisser à désirer, surtout si les pages originales ont été dactylographiées à l'aide d'un ruban usé ou si l'université nous a fait parvenir une photocopie de qualité inférieure.

La reproduction, même partielle, de cette microforme est soumise à la Loi canadienne sur le droit d'auteur, SRC 1970, c. C-30, et ses amendements subséquents.

NL-339 (r. 88/04) c

Canada

UNIVERSITY OF ALBERTA

SCATTER AND ATTENUATION CORRECTION TECHNIQUES FOR SINGLE PHOTON EMISSION COMPUTED TOMOGRAPHY

BY

TERENCE A. RIAUKA

A thesis submitted to the Faculty of Graduate Studies and Research in partial fulfillment of the requirements for the degree of Master of Science.

IN

MEDICAL PHYSICS

DEPARTMENT OF PHYSICS

EDMONTON, ALBERTA

FALL 1991

National Library of Canada
Bibliothèque nationale du Canada

Canadian Theses Service
Service des thèses canadiennes

Ottawa, Canada
K1A 0N4

The author has granted an irrevocable non-exclusive licence allowing the National Library of Canada to reproduce, loan, distribute or sell copies of his/her thesis by any means and in any form or format, making this thesis available to interested persons.

L'auteur a accordé une licence irrévocable et non exclusive permettant à la Bibliothèque nationale du Canada de reproduire, prêter, distribuer ou vendre des copies de sa thèse de quelque manière et sous quelque forme que ce soit pour mettre des exemplaires de cette thèse à la disposition des personnes intéressées.

The author retains ownership of the copyright in his/her thesis. Neither the thesis nor substantial extracts from it may be printed or otherwise reproduced without his/her permission.

L'auteur conserve la propriété du droit d'auteur qui protège sa thèse. Ni la thèse ni des extraits substantiels de celle-ci ne doivent être imprimés ou autrement reproduits sans son autorisation.

ISBN 0-315-69945-0

Canada

UNIVERSITY OF ALBERTA

RELEASE FORM

NAME OF AUTHOR: TERENCE A. RIAUKA

TITLE OF THESIS: SCATTER AND ATTENUATION CORRECTION TECHNIQUES FOR SINGLE PHOTON EMISSION COMPUTED TOMOGRAPHY

DEGREE: MASTER OF SCIENCE

YEAR THIS DEGREE GRANTED: 1991

Permission is hereby granted to the University of Alberta Library to reproduce single copies of this thesis and to lend or sell such copies for private, scholarly, or scientific research purposes only.

The author reserves all other publication and other rights in association with the copyright in the thesis, and except as hereinbefore provided neither the thesis nor any substantial portion thereof may be printed or otherwise reproduced in any material form whatever without the author's prior written permission.

Riauka

18112 - 96 Avenue

Edmonton, Alberta

T5T 3N3

August 26, 1991

UNIVERSITY OF ALBERTA

FACULTY OF GRADUATE STUDIES AND RESEARCH

The undersigned certify that they have read, and recommend to the Faculty of Graduate Studies and Research for acceptance, a thesis entitled SCATTER AND ATTENUATION CORRECTION TECHNIQUES FOR SINGLE PHOTON EMISSION COMPUTED TOMOGRAPHY submitted by Terence A. Riauka in partial fulfillment of the requirements for the degree of Master of Science in Medical Physics.

Dr. H. R. Hooper (Co – Supervisor)

Dr. Z. Gortel (Co – Supervisor)

Dr. R. Sloboda

Dr. L. Filipow

August 26, 1991

I dedicated this thesis in loving memory of my father, who provided me with the passion for knowledge and the motivation to achieve this goal.

Abstract

Scatter and attenuation correction methods were evaluated, for the traditional filtered backprojection method of reconstruction used in SPECT imaging. Two sets of experiments were performed. The first experiment was used to study the reduction of scatter in planar projection images, prior to reconstruction, using Compton window subtraction in conjunction with digital image filtering techniques. The second experiment was used to study attenuation correction methods applicable to the traditional filtered backprojection method of reconstruction.

The scatter component of the projections was reduced by using either a Metz filter or Compton window subtraction in conjunction with a Butterworth filter. The effects of attenuation on SPECT images were corrected by using either a preprocessing or an iterative post-processing attenuation correction method. For the iterative post-processing attenuation correction method, an iterative forward projection technique was investigated for different interpolation methods. The quantitative accuracy of the reconstructed transaxial slice images was evaluated by comparing them to a high count, high spatial resolution reference image using a specifically designed test which provided a quantitative measure of the similarity of an image with the reference image. It was found that the quantitative accuracy of the reconstructed transaxial images was substantially improved by the reduction of scatter in the planar projection images, and correcting for attenuation. However, both the scatter reduction and the attenuation correction techniques investigated lack robustness and, under certain circumstances, had detrimental effects on the images.

Acknowledgements

I wish to thank Dr. H.R. Hooper for his time and effort spent helping me prepare this thesis. I would also like to thank the Natural Sciences and Engineering Research Council of Canada for providing financial support through the PGS1 and the PGS2 Postgraduate Scholarships.

Contents

1 Introduction 1

2 Physics of Nuclear Medicine Imaging 3

3 The Anger Camera 6

3.1 Collimator 8

3.2 Scintillation Crystal 10

3.3 Photomultiplier Tube Assembly 10

3.4 Energy Circuits 11

3.5 Positioning Circuits 12

3.6 Correction Electronics and Algorithms 13

4 Filtered Back-Projection and SPECT 15

4.1 General 15

4.2 Mathematics of Computed Tomography 16

5 Application of Filtered Back-Projection 25

5.1 The MTF and Filters 25

5.2 Scatter and Attenuation 32

5.2.1 Scatter 32

5.2.2 Attenuation 34
5.3 Discrete Projections and Transforms 41
5.3.1 Linear Interpolation Weighting 44
5.3.2 Area Interpolation Weighting 45
5.3.3 Iterative Correction to Weighting 49
5.4 Image Comparison Techniques 50

6 Experiments **52**
6.1 Takahashi Phantom Study - Scatter Reduction/Compensation 52
6.1.1 Experiments 52
6.1.2 Image Processing Methods 55
6.2 Jaszczak Phantom Study - Attenuation Correction 58
6.2.1 Experiment 58
6.2.2 Image Processing Methods 59
6.3 Computer Simulation Experiment 62

7 Results **64**
7.1 Takahashi Phantom Results 64
7.2 Jaszczak Phantom Results 64
7.3 Computer Simulation Results 77

8 Discussion of Results **85**
8.1 Takahashi Phantom Results 85

8.2 Jaszczak Phantom Results 87

8.3 Computer Simulation Results 90

9 Conclusion **91**

9.1 Suggestions for Future Work 92

Bibliography **94**

List of Tables

6.1 Planar images (projections) obtained from the Takahashi phantom experiments. 56

7.1 The optimum k-value, k_o, for each set of image data for the three filtering methods. 67

7.2 A summary of the various parameters for each figure in Section 7.2. . . 68

List of Figures

3.1 A schematic diagram of the Anger camera. 7

4.1 The geometric relationship between the (x, y) and (t, s) coordinate systems. 17

4.2 A three dimensional matrix broken into two dimensional slices. 18

4.3 A one dimensional projection, $P_\phi(t)$, at an angle ϕ of the two dimensional distribution $f(x, y)$. 19

4.4 Graphical representation of the Fourier slice theorem. 23

5.1 The Butterworth filter for $\nu_c = 15.36$ pixels^{-1} and (**A**) $x_B = 7.5$, (**B**) $x_B = 12.5$, (**C**) $x_B = 17.5$. 28

5.2 The raw (**B**) and smoothed (**C**) one dimensional power spectra for a typical SPECT image, and the Metz filter (**A**) calculated for the image. 30

5.3 Metz filters for (**A**) $x_M = 2.5$, (**B**) $x_M = 4.0$, and (**C**) $x_M = 5.5$. 32

5.4 Attenuation lengths, $L_\phi(x, y)$, for an arbitrary reconstruction cell at (x,y). ..36

5.5 Pre-processing attenuation lengths, $\mathcal{L}_\phi(t)$. 38

5.6 Post-processing attenuation lengths, $L_\phi(x_0, y_0)$. 40

5.7 The geometry for the linear interpolation weighting. 43

5.8 The geometry for the area interpolation weighting. 46

5.9 Blow-up of one reconstruction cell for the area interpolation weighting. 47

6.1 Schematic diagram of the Takahashi phantom. 53

6.2 The experimental set-up for the Takahashi phantom experiment. 54

6.3 The experimental set-up for the Jaszczak phantom experiment. 58

6.4 The computer generated, noiseless slice used for testing the interpolation methods. 63

7.1 The improvement indices for Compton window subtraction prior to Metz filtering, as a function of the fraction k, for fixed x_M and variable x_M. 65

7.2 The improvement indices for Compton window subtraction prior to Butterworth filtering, as a function of the fraction k. 66

7.3 The improvement indices for the two attenuation corrections methods and the two filtering methods. 69

7.4 The improvement indices, as a function of the enlargement of one of the boundary's axis, for the post-processing and the pre-processing attenuation correction methods. 71

7.5 The profiles for the reconstructed image for various enlarged boundaries. ... 72

7.6 The improvement indices, as a function of the shift distance of the boundary, for the post-processing and the pre-processing attenuation correction methods. 73

7.7 The profiles for reconstructed images for various shifted boundaries. 74

7.8 The improvement indices, as a function of the number of iterations for the iterative post-processing attenuation correction method combined with the iterative forward projection technique using the exact boundary. 75

7.9 The improvement indices, as a function of the number of iterations for the iterative post-processing attenuation correction method combined with the iterative forward projection technique using a boundary enlarged by 2 pixels. 76

7.10 The profiles for the reconstructed image using the iterative post-processing attenuation correction method and no iterations in the iterative forward projection for a boundary enlarged by 1 pixel, 3 pixels, and 5 pixels. 78

7.11 Same as figure 7.10 except one iteration of the iterative forward projection technique was performed for each iteration of the iterative post-processing attenuation correction. 79

7.12 Same as figure 7.10 except two iterations of the iterative forward projection technique were performed for each iteration of the iterative post-processing attenuation correction. 80

7.13 The profiles for the reconstructed image using the iterative post-processing attenuation correction method and no iterations of the iterative forward projection technique for a boundary shifted by 1 pixel, 2 pixels, and 3 pixels. ..81

7.14 Same as figure 7.13 except one iteration of the iterative forward projection technique was performed for each iteration of the iterative post-processing attenuation correction. 82

7.15 Same as figure 7.13 except two iterations of the iterative forward projection technique were performed for each iteration of the iterative post-processing attenuation correction. 83

7.16 The convergence of reproduced images to the original image, based on the ψ-comparison index, as a function of the number of iterations of iterative forward projection. 84

Chapter 1

Introduction

Single Photon Emission Computed Tomography (SPECT) imaging has become an important diagnostic medical procedure performed in Nuclear Medicine departments. The images acquired from these procedures are unique in that they provide physicians with a three dimensional map which reflects the metabolism of an administered pharmaceutical within a patient. The map is obtained by labeling the pharmaceutical with a radioactive element, such as Technetium 99m, that decays through the emission of photons. The emitted photons are recorded by a special detector system, called the Anger camera, and recorded events are processed to produce a three dimensional representation of the distribution of the pharmaceutical.

Of particular importance and interest in Nuclear Medicine is to correct for Compton scattering and photoelectric absorption of the emitted photons within the patient's body. Both of the processes reduce the quantitative accuracy of the acquired images. The inclusion of Compton scattered photons causes the images to be blurred. Both Compton scattering and photoelectric absorption causes a relative loss of information (counts) from regions deeper in a patient's body, a process referred to as attenuation.

Techniques used to compensate for Compton scattering and attenuation, that

fall under the traditional filtered back projection method of reconstruction, generally improve the qualitative appearance of the images. In this work, these methods are evaluated to determine their quantitative accuracy and robustness in the clinical situation.

The thesis will begin with an introduction to the physics of Nuclear Medicine imaging and problems specific to this type of imaging in Chapter 2. Chapter 3 discusses the components of the Anger camera and their performance for Nuclear Medicine imaging. The mathematics of the traditional filtered back-projection method of reconstruction is presented in Chapter 4. Chapter 5 describes the application of the traditional filtered back-projection method of reconstruction to SPECT. In particular, the equations of the traditional filtered backprojection method of reconstruction are digitized, and methods for scatter compensation and attenuation correction are described. An image evaluation technique, designed to quantitatively evaluate SPECT images, is also discussed. In Chapter 6, a set of experiments, performed to investigate the effects of scatter and attenuation in SPECT imaging, are described. In Chapter 7, the scatter compensation and attenuation correction methods are evaluated and results are presented. A discussion of the results for the scatter compensation and attenuation correction methods is given in Chapter 8. In Chapter 9 the conclusions are summarized and suggestions for future work are presented.

Chapter 2

Physics of Nuclear Medicine Imaging

Nuclear Medicine is the medical specialty in which radioactive materials are used to diagnose and treat a wide variety of diseases and disorders. In Nuclear Medicine a patient is given a small quantity of a radiopharmaceutical, consisting of a radionuclide attached, in most instances, to a drug or chemical. The radiopharmaceutical is distributed throughout the patient's body (or specific regions of the body) based upon the pharmacologic properties it possesses. The radioactive elements used in Nuclear Medicine imaging decay by releasing (emitting) gamma-rays (photons) of specific energies. The emitted gamma-rays are detected using a specially designed gamma detector system called the gamma, scintillation, or Anger camera. The data from the detector is processed to produce an image which represents the spatial distribution of the radiopharmaceutical. The image is a record of how the radiopharmaceutical was metabolized by the patient. As such, Nuclear Medicine measures the functioning of body tissues and organs and not just their morphology.

The radiopharmaceutical quantities used in Nuclear Medicine imaging procedures contain only small amounts of radioactivity. The amount of activity that a patient is given, in a single dose, ranges from 250 to 1500 MBq, depending upon the imaging situation. From this activity the patient typically receives a whole body

radiation dose of about 500 μSv (50 mrads).

The radioactive materials used to label the pharmaceutical are single photon emitters. The photons are emitted isotropically and generally range in energy from 71keV for Tl201 to 365keV for I131, with Tc99m at 140keV being the most popular for Nuclear Medicine procedures. Photons with these energies interact with body tissues primarily through two interactions, Compton scattering and photoelectric absorption. Both of these processes lead to attenuation of the emitted photons, and account for some of the radiation dose received by the patient. Both processes are also random in nature, with the probability of an event occurring being proportional to $(1 - e^{-\mu t})$, where t is the thickness of the material which the photon must transverse to reach the detector, and μ is the cross section for either Compton scattering or photoelectric absorption.

In Compton Scattering, the photon is scattered by a loosely bound orbital electron. The amount of energy that the photon transfers to the electron is dependent upon the scattering angle of the photon with respect to its incident direction. Mathematically the energy of the photon after scattering is given as

$$E_{\text{After}} = \frac{E_{\text{Initial}}}{1 + \frac{E_{\text{Initial}}}{m_0 c^2}(1 - \cos\phi)}, \tag{2.0.1}$$

where m_0c^2 is the electron rest energy and ϕ is the photon scattering angle. For small scattering angles the photons lose very little energy. As will be noted in the next chapter, gamma cameras cannot discriminate between photons scattered through small scattering angles and unscattered photons. The scattered photons

are mis-positioned in images, and thus degrade both the qualitative appearance and the quantitative accuracy of these images.

In photoelectric absorption an emitted photon loses all of its energy to an orbital electron. When this occurs within the patient, the photon is not detected by the camera. Since this attenuation is more likely to occur for regions deep in the body than for surface regions, the problem of measuring the relative uptake of the radioactivity throughout the body becomes more complicated.

Chapter 3

The Anger Camera

Detector systems used in Nuclear Medicine imaging are designed to detect the spatial location at which an incident photon strikes the detector. The most commonly used system was developed by Anger in 1958 and is called a gamma or Anger camera. A schematic diagram of the Anger camera is shown in figure 3.1. Although many improvements have been made to the Anger camera since its development, the basic components of the camera remain unchanged. In this chapter the performance and the physical limitations of the Anger camera and its components are reviewed.

Various parameters are used to specify the performance of the detector system, including spatial resolution, energy resolution and sensitivity.

The spatial resolution of the detector is a measure of how far apart two sources must be separated to be detected as distinct. A small source does not appear as a single point in an image but as a *bell-shaped* distribution of points spread over a region; i.e. with the intensity of counts greatest at the center and falling off towards the edges. The full width at half maximum (FWHM) is a measure of the distance across this distribution at an intensity of 50% of the maximum. Spatial resolution is usually measured using the FWHM, which represents the minimum spatial separation required for two sources to be detected as distinct. This parameter

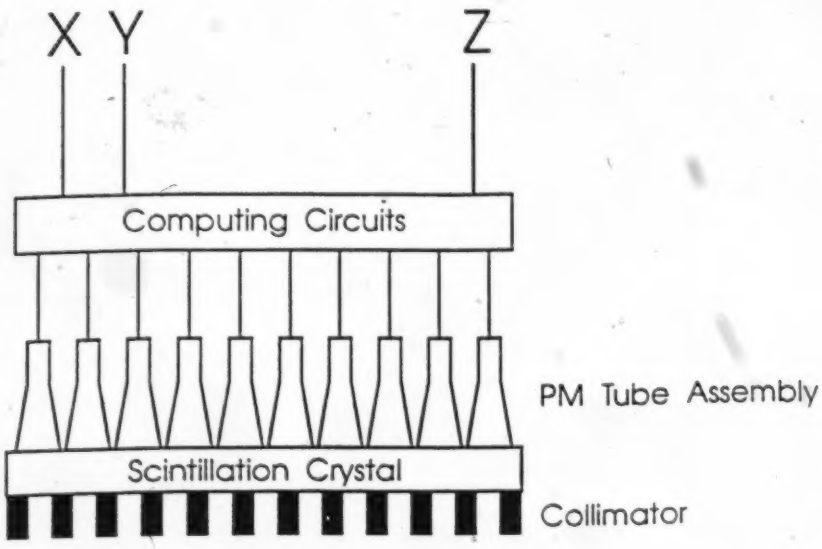

Figure 3.1: A schematic diagram of the Anger camera.

is dependent upon the energy of the sources, the distance of the sources from the detector, and the type and the thickness of material separating the sources and the detector.

The energy resolution is a measure of the extent to which the detector can distinguish between two sources of differing energy or, two energies emitted by one source. The energy response of the system for a monoenergetic source is not a delta function, but rather a Gaussian shaped distribution of energies. The FWHM of the energy spectrum for a monoenergetic source indicates the minimum energy difference required to separate photon sources with different energies.

The sensitivity of a detector is defined as the number of gamma-rays detected by the Anger camera per unit of radioactivity present. Sensitivity can generally

be expressed as the product of two terms; the geometric efficiency of the detector, which measures the fraction of emitted photons that actually enter the detector, and an intrinsic efficiency, which specifies what fraction of the photons entering the detector are actually recognized and recorded by the system.

3.1 Collimator

The scintillation crystal is very sensitive to incident photons but has no directional discrimination. The collimator provides the detector with directional discrimination by allowing only those photons traveling in the appropriate directions to reach the detector. Photons not traveling in the appropriate directions are absorbed by the collimator. The collimator is made of photon absorbing material, such as lead foil or tungsten, with a regular pattern of holes formed in it.

The most common collimator for SPECT procedures is the parallel hole collimator, in which the holes are formed perpendicular to the face of the scintillation crystal. This collimator allows only those photons whose direction of travel is nearly perpendicular to the face of the crystal to pass, while absorbing all others. The collimator's design partly determines the spatial resolution of the detector and affects it's sensitivity. The acceptance angle, α, for the parallel hole collimator is given by

$$\alpha = 2\tan^{-1}\frac{d}{2l_e} \tag{3.1.1}$$

where d is the diameter of the holes and l_e is the effective hole length and is given

as

$$l_e = l - 2\mu^{-1} \qquad (3.1.2)$$

where l is the physical hole length and μ is the linear attenuation coefficient of the collimator material at the photon energy. The effective length accounts for the penetration of the photons through the collimator walls, or septa, surrounding the holes. The spatial resolution of the collimator is dependent on the acceptance angle and the source to collimator distance. The sensitivity of the collimator is dependent both on the acceptance angle and the ratio of septal thickness to hole diameter, but is independent of the source to collimator distance for parallel hole collimators. A compromise between good spatial resolution and good sensitivity must be made when deciding on the collimator for a given imaging situation. Low energy parallel hole collimators generally come in three designs: high resolution, high sensitivity, and all purpose. The difference between the collimators is the number, length and diameter of the holes in the collimator.

The collimator is designed for a particular energy range. As the energy increases the thickness of the collimator material must increase to absorb the incident photons efficiently. To obtain the same sensitivity for higher energies, the holes are formed with a larger diameter, to keep the ratio of septal thickness to hole diameter constant. Parallel hole collimators are generally designed for three energy ranges: low (<160keV), medium (160-300keV), and high (300-400keV).

3.2 Scintillation Crystal

The crystal determines the sensitive area of the detector. For Nuclear Medicine procedures a detector with a sensitive area capable of covering a large portion of the human body is desirable. The main function of the scintillation crystal is to absorb an incident photon and convert it into a large number of scintillation photons. The crystal must have a relatively high atomic number to be a good absorber of photons in the energy range of interest in nuclear medicine (70-370keV).

The scintillation crystal used in the Anger camera is a thallium activated sodium iodide (NaI(Tl)) single crystal. The crystals may provide a rectangular or circular field of view. Their sizes range from 30 to 50cm in diameter for circular and 40×22 to $50\times40cm^2$ for rectangular. The thickness of the crystal ranges from 0.60 to 1.25 cm. Sodium iodide is used because of iodine's relatively high atomic number and hence good photon absorption properties. The NaI crystal is hermetically sealed by aluminum ($\approx$ 1mm thick), with a glass exit window at the back, to protect the crystal from stray light and water vapor. The inside surface of the aluminum is coated with white aluminum oxide to reflect the scintillation photons toward the back of the detector.

3.3 Photomultiplier Tube Assembly

The scintillation crystal is backed up by an assembly of photomultiplier tubes (PMT). Depending on the size of the crystal, the number of PMTs ranges from

37 to 91. The PMTs may be round or hexagonal and range in size from 5 to 7.5 cm in diameter. The PMTs are arranged in a hexagonal close-packed arrangement.

The PMTs detect scintillation photons and produce an electronic signal. A scintillation photon absorbed on the photocathode of the PMT will cause an electron to be liberated. The liberated electron is accelerated towards the first dynode of the PMT and upon collision liberates 3 to 5 more electrons. This process continues down the chain of 10 to 12 dynodes. A single electron from the photocathode causes an avalanche of electrons at the anode, due to this multiplication process. The signal (pulse) that comes off the anode is of the order of 10^{-9} volts, and is proportional to the number of scintillation photons absorbed over a short time period by the photocathode. This signal is too small to be processed by the electronics of the detector and must be amplified.

3.4 Energy Circuits

To determine the energy of the incident photon, the pulses from all PMTs are summed into one signal, called the Z-signal. The amplitude of the Z-signal represents the energy deposited in the crystal by the incident photon. However, this amplitude fluctuates for identical incident photons due to the random nature of the processes involved. Any photon interacting with the crystal will produce a flash of scintillation photons. The number of scintillation photons produced is on average proportional to the energy deposited by the incident photon and follows a Poisson

distribution. For every 100keV of energy deposited about 13keV of scintillation photons are produce [Cr86]. The scintillation photons have an energy of about 3eV. Therefore, approximately 4,300 scintillation photons are produced for every 100keV deposited (or about 6000 for Tc99m). A certain percentage of these scintillation photons will liberate a photoelectron; usually about 1 photoelectron is produced for every four scintillation photons absorbed on the photocathode of the PMT [An84]. The pulse coming off the anode of the PMT is also random, due to the random nature of the dynode multiplication process. These processes, when summed over all the PMTs, account for the relatively poor energy resolution of the Anger camera. The FWHM of the energy spectrum for the 140 keV photons of ^{99m}Tc is typically 17 keV.

The energy window is a predefined range of energies for which the system will record an event. All events with energies outside the energy window are ignored by the system. The energy windows used in Nuclear Medicine depend on the imaging conditions but are usually of the order of 10 to 20 percent of the emission energy, and are centered on the emission energy.

3.5 Positioning Circuits

Each photon that is absorbed in the scintillation crystal produces a flash of many scintillation photons. Each PMT will see a certain percentage of these scintillation photons depending on the PMT's distance from the location of interaction. The

signals from all the PMTs are summed, with appropriate weighting factors, to produce four analog signals; X^-,X^+,Y^-,and Y^+. The location signals (X, Y) and total energy signal (Z) of the interaction are obtained as

$$Z = X^+ + X^- + Y^+ + Y^- \tag{3.5.1}$$

$$X = \frac{k}{Z}(X^+ - X^-) \tag{3.5.2}$$

$$Y = \frac{k}{Z}(Y^+ - Y^-) \tag{3.5.3}$$

where k is a scaling constant. The coordinates of the interaction location in the crystal are directly proportional to the position signals (X, Y).

There is always a small error in the location of the interaction determined by the system. The intrinsic spatial resolution of the detector is a measure of this error. The intrinsic spatial resolution depends primarily on the average number of scintillation photons detected by the PMTs closest to the location of the interaction event. The larger the number of scintillation photons detected, the lower the statistical error in each tube's output, and hence the better the intrinsic spatial resolution. The ability of the PMTs to detect the scintillation photons depends on several factors, including the number, size, quality and geometry of the PMTs, and the crystal thickness.

3.6 Correction Electronics and Algorithms

The components of the Anger camera must be tuned to respond uniformly and linearly. This can be accomplished by physically tuning the components (i.e. increasing or decreasing voltages, or replacing faulty components). However, even

the best tuned camera is inherently nonlinear. Thus, all modern cameras employ correction electronics and dedicated microprocessors to compensate for spatial distortions and variations in the energy response at different locations in the camera's field-of-view. These electronics compensate for nonlinearities and nonuniformities by adjusting the response of the components based on previously performed calibration procedures.

Chapter 4

Filtered Back-Projection and SPECT

4.1 General

Single Photon Emission Computed Tomography (SPECT) is a special imaging procedure performed in Nuclear Medicine. In SPECT, a three dimensional distribution of radioactivity is reconstructed from a set of two dimensional projections through the application of tomographic reconstruction techniques. The basic mathematics of computed tomography was developed by Radon in 1917 with applications to gravitational fields. Due to the fact that Radon's work was related to gravitational fields and written in German it remained unnoticed by English researchers and has been rediscovered by numerous researchers in different fields. These equations, and the solutions to these equations, were rediscovered by Bracewell in 1956 with applications to radioastronomy. In 1963 Cormack developed and applied similar mathematics to radiology.

The basic problem involves reconstructing a function from a set of line integrals through that function. In SPECT the line integrals are the projections of a three dimensional (3D) distribution of radioactivity and the function is the 3D distribution of the radioactivity. As will be shown, this amounts to inverting an integral

equation. It was not until computers became commonplace that such inversions could be calculated readily. Even though the solution to the problem is known analytically, calculating it is complicated by several factors. These factors arise from the physical processes involved and the physical limitations of the detector system. In this chapter the general problem and solutions to it are applied to SPECT.

In SPECT studies, N projections of the distribution of radioactivity are obtained using the Anger camera. The projections are 2D (i.e. images) and are obtained at regular angular intervals about an axis of rotation. The mathematical problem is to calculate the 3D distribution $f(x, y, z)$ from a set of its projections, $P_{\phi_i}(t, z)$ $(i = 1, \cdots, N)$, where ϕ and t are defined in figure 4.1. The 3D distribution will be considered to be made up of 2D planar slices, $f_z(x, y)$, as shown in figure 4.2.

By reconstructing each of the planar slices the 3D distribution is obtained. In this approximation the slices can be regarded as distinct and having no dependence on each other. Each row in the 2D projection, $P_{\phi_i}(t, z = \text{constant})$, obtained by the gamma camera can be regarded as the 1D projection, $P_{\phi_i}(t)$, of a planar slice, $f(x, y)$. Based on this model of reconstruction the problem reduces to finding the 2D slices from the 1D projections of these slices.

4.2 Mathematics of Computed Tomography

A 1D projection of a 2D distribution, $f(x, y)$, for a given ϕ as a function of t is shown in figure 4.3. The 1D projection, $P_\phi(t)$, is given mathematically by

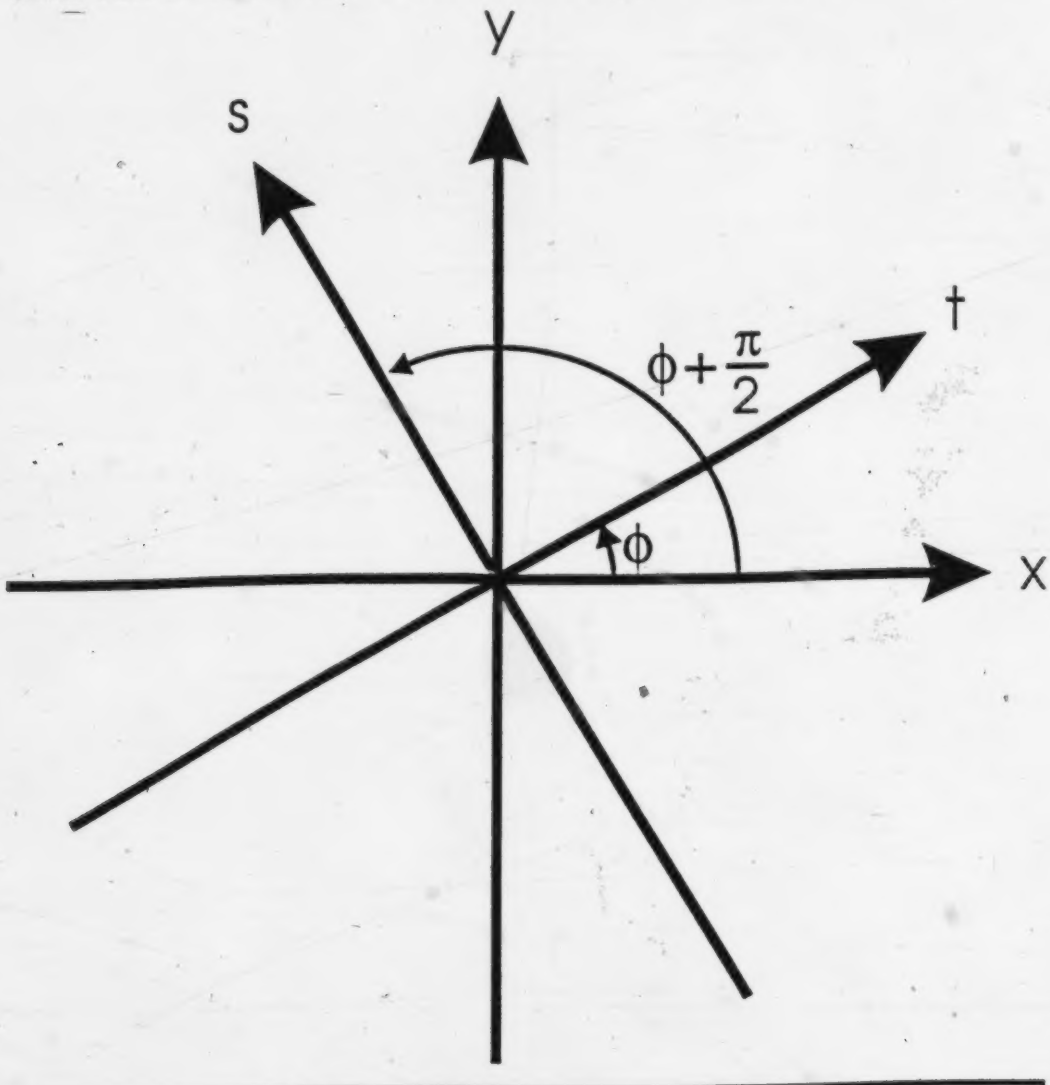

Figure 4.1: The geometric relationship between the (x, y) and (t, s) coordinate systems. The z-axis is directed out of the page.

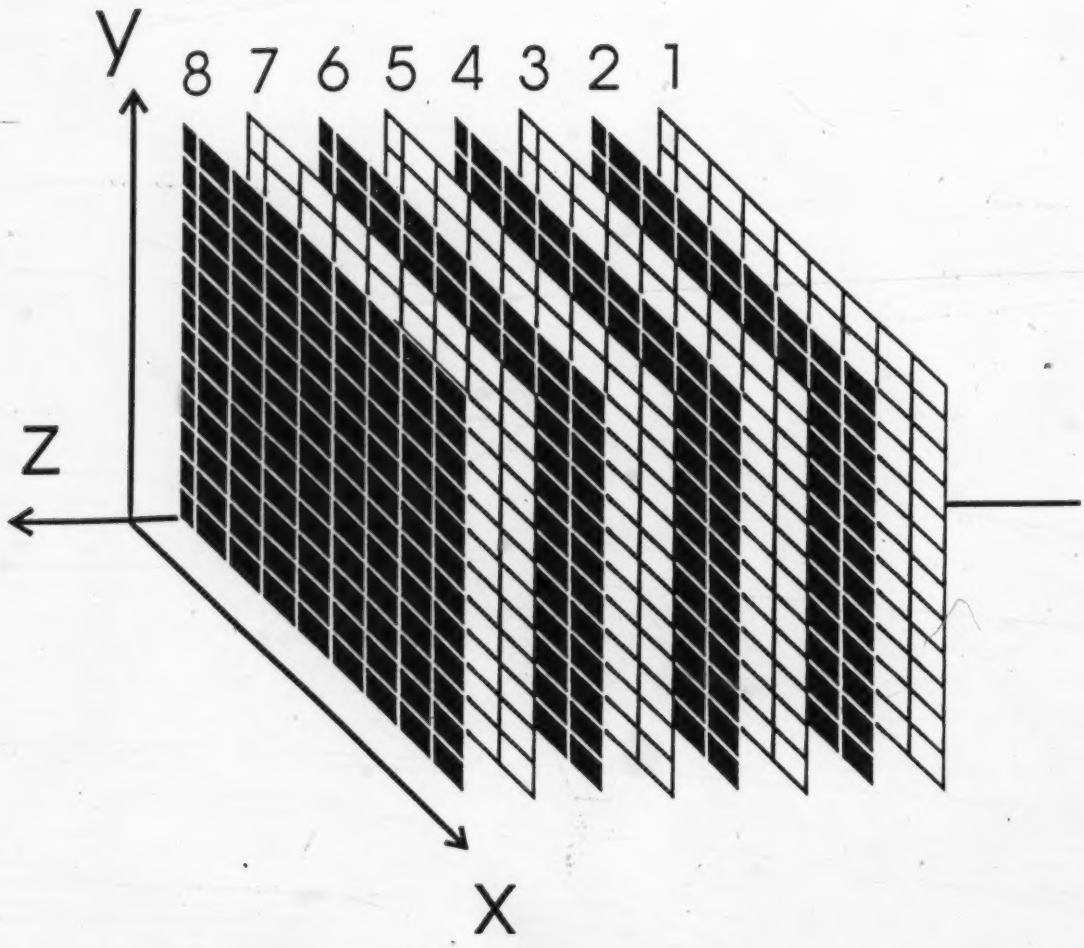

Figure 4.2: A three dimensional matrix broken into two dimensional slices.

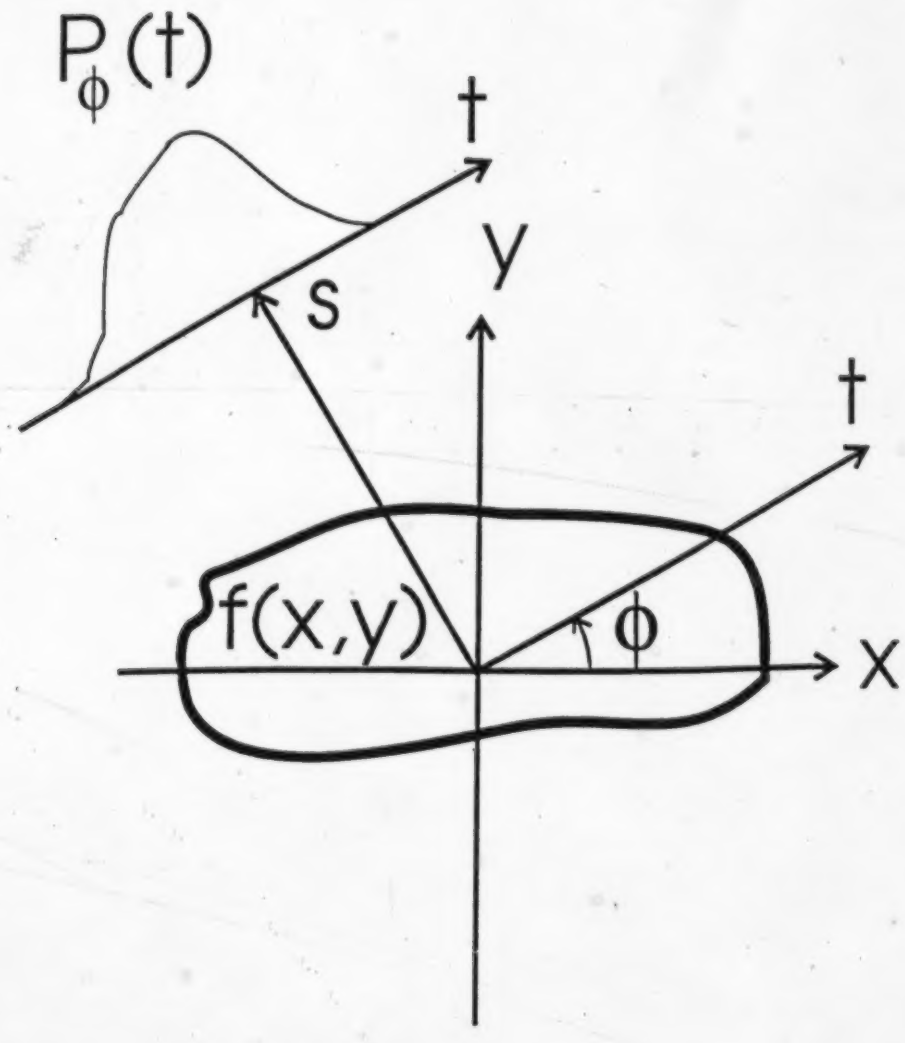

Figure 4.3: A one dimensional projection, $P_\phi(t)$, at an angle ϕ of the two dimensional distribution $f(x,y)$.

$$P_\phi(t) = \int_{(\phi,t)_{\text{line}}} f(x,y)\, ds, \tag{4.2.1}$$

where the integral is evaluated along the line defined by ϕ and t. By employing the properties of the δ-function the above integral can be expressed as

$$P_\phi(t) = \int_{-\infty}^{\infty}\int_{-\infty}^{\infty} f(x,y)\delta(x\cos\phi + y\sin\phi - t)dxdy, \tag{4.2.2}$$

where $P_\phi(t)$ is termed the Radon transform of the function $f(x,y)$. Equation (4.2.2) cannot be inverted analytically in coordinate space to obtain the image, $f(x,y)$, from the known projections, $P_\phi(t)$. Instead, consider the 2D Fourier Transform (FT) of the object $f(x,y)$, given as

$$F(u,v) = \int_{-\infty}^{\infty}\int_{-\infty}^{\infty} f(x,y)e^{-i2\pi(ux+vy)}dxdy, \tag{4.2.3}$$

and the FT of a projection at an angle ϕ, given as

$$S_\phi(\omega) = \int_{-\infty}^{\infty} P_\phi(t)e^{-i2\pi\omega t}dt, \tag{4.2.4}$$

where $t = x\cos\phi + y\sin\phi$, and u and v of Eq(4.2.3) are related to ω and ϕ through $u = \omega\cos\phi$ and $v = \omega\sin\phi$. The FT of $f(x,y)$ for $v = 0$ is

$$\begin{aligned} F(u, v=0) &= \int_{-\infty}^{\infty}\int_{-\infty}^{\infty} f(x,y)e^{-i2\pi ux}dxdy & (4.2.5)\\ &= \int_{-\infty}^{\infty}\left[\int_{-\infty}^{\infty} f(x,y)dy\right]e^{-i2\pi ux}dx, & (4.2.6)\end{aligned}$$

where the term in brackets is the projection of $f(x,y)$ at angle $\phi = 0$. Similarly, the FT of $f(x,y)$ for $u = 0$ is

$$\begin{aligned} F(u=0, v) &= \int_{-\infty}^{\infty}\int_{-\infty}^{\infty} f(x,y)e^{-i2\pi vy}dxdy & (4.2.7)\\ &= \int_{-\infty}^{\infty}\left[\int_{-\infty}^{\infty} f(x,y)dx\right]e^{-i2\pi vy}dy, & (4.2.8)\end{aligned}$$

where the term in brackets is now the projection of $f(x,y)$ at angle $\phi = \pi/2$. Equations (4.2.6) and (4.2.8) provide the identities

$$F(u, v=0) = \int_{-\infty}^{\infty} P_{\phi=0}(t=x)e^{-i2\pi ux}dx = S_{\phi=0}(u) \tag{4.2.9}$$

$$F(u=0, v) = \int_{-\infty}^{\infty} P_{\phi=\pi/2}(t=y)e^{-i2\pi vy}dy = S_{\phi=\pi/2}(v). \tag{4.2.10}$$

As will be shown below, the FT of a projection at any angle ϕ gives a slice of the 2D FT of the image, $f(x,y)$, at the same angle ϕ in Fourier space. This is known as the Fourier slice theorem and is central to the reconstruction of a distribution, using the filtered back-projection technique.

The Fourier slice theorem can be derived by considering the related (t,s)-coordinate system. The (x,y) and (t,s) coordinate systems are related through the transformation

$$\begin{pmatrix} t \\ s \end{pmatrix} = \begin{pmatrix} \cos\phi & \sin\phi \\ -\sin\phi & \cos\phi \end{pmatrix} \begin{pmatrix} x \\ y \end{pmatrix}. \tag{4.2.11}$$

In the (t,s)-coordinate system projections along lines of constant t are written as

$$P_\phi(t) = \int_{-\infty}^{\infty} f(t,s)ds, \tag{4.2.12}$$

and the FT of the projections is

$$S_\phi(\omega) = \int_{-\infty}^{\infty} P_\phi(t)e^{-i2\pi\omega t}dt \tag{4.2.13}$$

$$= \int_{-\infty}^{\infty} \left[\int_{-\infty}^{\infty} f(t,s)ds\right] e^{-i2\pi\omega t}dt. \tag{4.2.14}$$

Substituting back to the (x,y)-coordinate system gives Eq(4.2.14) as

$$S_\phi(\omega) = \int_{-\infty}^{\infty}\int_{-\infty}^{\infty} f(x,y)e^{-i2\pi\omega(x\cos\phi + y\sin\phi)}dxdy = F(\omega\cos\phi, \omega\sin\phi). \tag{4.2.15}$$

The last equation demonstrates that $S_\phi(\omega)$ is a slice of $F(u,v)$, the 2D FT of $f(x,y)$, for the frequencies $u = \omega\cos\phi$ and $v = \omega\sin\phi$. This is shown graphically in figure 4.4.

The power of the Fourier slice theorem is that the distribution $f(x,y)$ can be obtained from the complete set of projections $P_\phi(t)$ by inverse Fourier transforming $F(u,v)$,

$$f(x,y) = \int_{-\infty}^{\infty}\int_{-\infty}^{\infty} F(u,v)e^{i2\pi(ux+vy)}dudv. \tag{4.2.16}$$

Transforming to $u = \omega\cos\phi$ and $v = \omega\sin\phi$, substituting $S_\phi(\omega) = F(\omega\cos\phi,\omega\sin\phi)$ from Eq(4.2.15), and using $dudv = \omega d\omega d\phi$, Eq(4.2.16) may be rewritten as

$$f(x,y) = \int_0^{2\pi}\int_{-\infty}^{\infty} S_\phi(\omega)e^{i2\pi\omega(x\cos\phi+y\sin\phi)}\omega d\omega d\phi. \tag{4.2.17}$$

The last equation can be obtained in a form that is more suitable for computer implementation by employing the symmetry of $P_\phi(t)$, and therefore, also $S_\phi(\omega)$. Namely, $S_{\phi+\pi}(\omega) = -S_\phi(-\omega)$, which allows Eq(4.2.17) to be rewritten as

$$f(x,y) = \int_0^{\pi}\left[\int_{-\infty}^{\infty} S_\phi(\omega)|\omega|e^{i2\pi\omega t}d\omega\right]d\phi \tag{4.2.18}$$

$$= \int_0^{\pi} Q_\phi(t)d\phi \tag{4.2.19}$$

where

$$Q_\phi(t) = \int_{-\infty}^{\infty} S_\phi(\omega)|\omega|e^{i2\pi\omega t}d\omega \tag{4.2.20}$$

$$= \int_{-\infty}^{\infty}\left[\int_{-\infty}^{\infty} P_\phi(t')e^{-i2\pi\omega t'}dt'\right]|\omega|e^{i2\pi\omega t}d\omega. \tag{4.2.21}$$

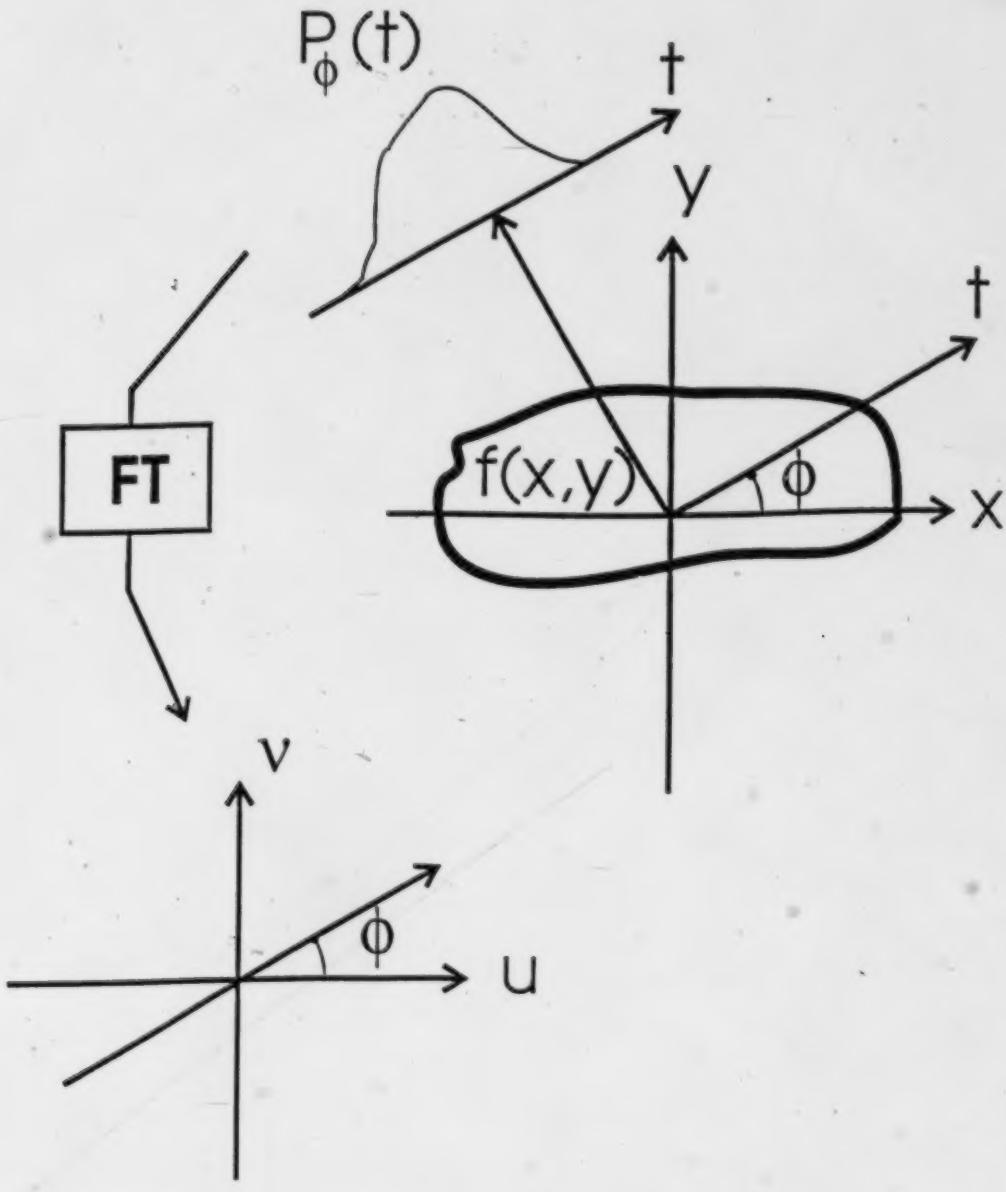

Figure 4.4: Graphical representation of the Fourier slice theorem.

$Q_\phi(t)$ is termed the filtered transform projection. The $|\omega|$-term in Eq(4.2.21) is called the ramp filter which removes the artifacts that are produced when the original projections $P_\phi(t)$ are back-projected directly [i.e. $Q_\phi(t) \rightarrow P_\phi(t)$ in Eq(4.2.19)]. The above method of reconstruction is termed the filtered back-projection method of reconstruction [He80, Ah89, Ka88a].

Chapter 5

Application of Filtered Back-Projection

The mathematical theory just presented requires some assumptions and approximations for application to SPECT. SPECT imaging has many physical and intrinsic limitations which impede the ability to quantitatively reconstruct images. The four predominant problems encountered in SPECT are: 1) attenuation, 2) scatter, 3) statistical noise, and 4) instrument response - all of which lead to image degradation. In employing the filtered back-projection method of reconstruction the latter three problems are partially compensated for by filtering. The first is compensated for using attenuation correction techniques.

The most apparent physical limitations of SPECT are: 1) projections are digitized, 2) count rates are low, 3) poor spatial and energy resolution, and 4) instrument response is dependent on particular imaging conditions. Each of these limitations and problems will be discussed and methods for compensation will be explored in the following sections.

5.1 The MTF and Filters

The discussion of reconstruction in the preceding chapter neglects the fact that the projections $P_\phi(t)$ obtained are not simple line integrals of the distribution $f(x,y)$,

but are convolved with an instrument (or response) function. The instrument function is dependent upon the amount and the geometry of the scatter material, and the energy and the distribution of the source. The instrument function's effect on the raw projections can be approximated as

$$P'_\phi(t) = P_\phi(t) * h(t,\phi), \tag{5.1.1}$$

where $P_\phi(t)$ are the true line integrals, $P'_\phi(t)$ are the line integrals measured by the camera system, $h(t,\phi)$ is the instrument function, and $*$ is the convolution operator. The effects of the instrument function on raw data can be removed by considering the FT of the above equation,

$$\mathcal{F}[P'_\phi(t)] = \mathcal{F}[P_\phi(t) * h(t,\phi)] = \mathcal{F}[P_\phi(t)] \cdot \mathcal{F}[h(t,\phi)] \tag{5.1.2}$$

and therefore

$$\mathcal{F}[P_\phi(t)] = \frac{\mathcal{F}[P'_\phi(t)]}{\mathcal{F}[h(t,\phi)]}. \tag{5.1.3}$$

where $\mathcal{F}[h(t,o)]$, called the modulation transfer function (MTF) of the system, characterizes instrument response as a function of spatial frequency. To account for the instrument function, Eq.(4.2.21) must be modified as

$$Q_\phi(t) = \int_{-\infty}^{\infty} \left[\int_{-\infty}^{\infty} P'_\phi(t') e^{-i2\pi\omega t'} dt' \right] |\omega| H_\phi(\omega) e^{i2\pi\omega t} d\omega, \tag{5.1.4}$$

where

$$H_\phi(\omega) = \text{MTF}^{-1} = \frac{1}{\mathcal{F}[h(t,\phi)]} = \text{Filter}. \tag{5.1.5}$$

Generally the filter function, $H_\phi(\omega)$, is chosen to enhance or suppress some feature of the projections and so does not necessarily represent the inverse of the MTF.

In particular, the high spatial frequencies of a SPECT image are dominated by noise, whereas the low spatial frequencies are suppressed due to the instrument response. Two filter functions will be considered in this thesis.

The first is the commonly used Butterworth filter which suppresses noise by allowing only the low frequency components of the image to pass. The Butterworth is a low pass filter, expressed mathematically as

$$H(\nu) = \frac{1}{\sqrt{1 + \left(\frac{\nu}{\nu_c}\right)^{x_B}}} \tag{5.1.6}$$

where ν_c is the cut-off frequency, usually expressed as a fraction of the Nyquist frequency, ν_N, and x_B is the roll-off parameter. For images of size 64*64, ν_N = 32.0 pixels^{-1}. The Butterworth filters for $\nu_c = 0.48 \cdot \nu_N$ and various values of x_B are shown in figure 5.1. This filter function is not directly dependent upon the MTF of the system, although the parameters ν_c and x_B are usually chosen with the system MTF in mind.

The second filter is the Metz filter. The Metz is both a resolution recovery and noise suppression filter which depends both on the power spectrum of the image to be filtered and the MTF of the system. The Metz filter is capable of enhancing (recovering) low frequency components while suppressing noise at higher frequencies, and is given by

$$H(\nu) = \frac{[1 - (1 - \mathrm{MTF}^2(\nu))^{x_M}]}{\mathrm{MTF}(\nu)}. \tag{5.1.7}$$

The MTF is sometimes modelled by a two parameter pseudo-gaussian, which is

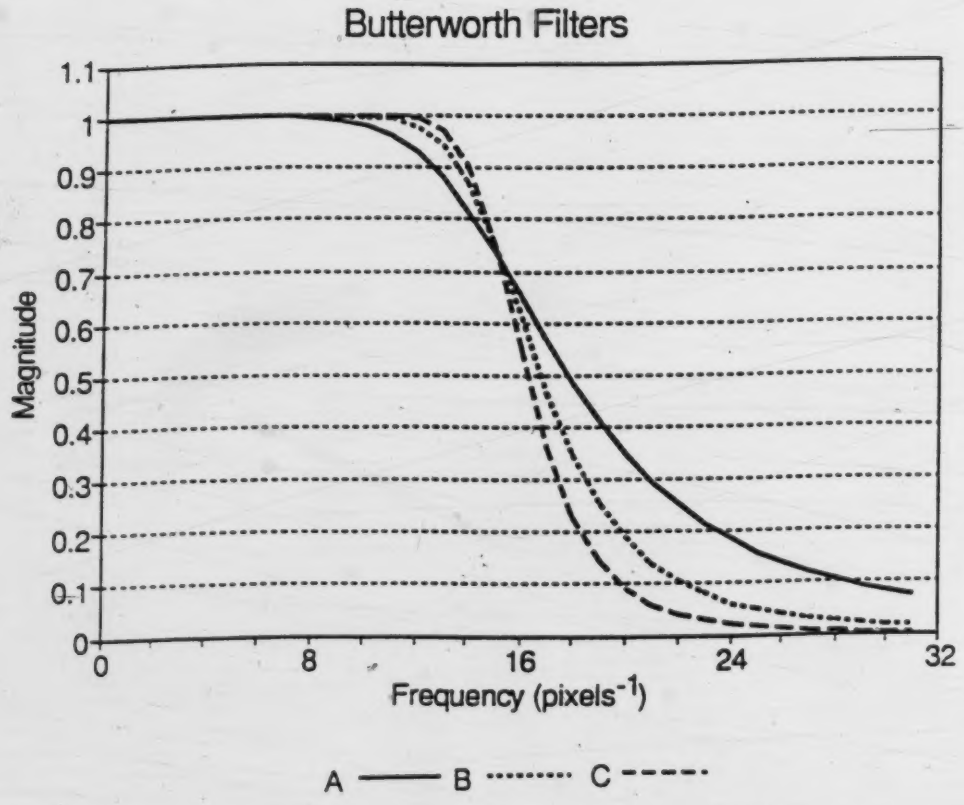

Figure 5.1: The Butterworth filter for $\nu_c = 15.36$ pixels^{-1} and (A) $x_B = 7.5$, (B) $x_B = 12.5$, (C) $x_B = 17.5$.

based on an experimentally determined MTF, and can be expressed as

$$\mathrm{MTF}(\nu) = e^{-\frac{\nu P}{S}}. \tag{5.1.8}$$

The parameters P and S are dependent on the amount of scatter material present, source to camera distance, and source geometry and energy. The parameter x_M in Eq(5.1.7) controls the extent to which the filter follows the inverse of the MTF before the low-pass portion of the filter (numerator of Eq(5.1.7)) dominates [Ki84, Ki87]. The optimum value for x_M for a given image is found by considering the 1D collapsed (or compressed) power spectrum of the image [Ki87]. The power spectrum for a 2D image is calculated and collapsed, assuming radial symmetry, to 1D. The Metz filter for an image is constructed by finding the lowest spatial frequency at which the power spectrum of the image is dominated by noise. The parameter x_M is determined from the constraint that the filter equal unity at the highest spatial frequency where the power spectrum is approximately ten times greater than the high frequency noise level.

In practice, fluctuations in the power spectrum as a function of frequency may complicate both the determination of the noise level and the frequency at which the power spectrum is ten times greater than the noise level. To minimize this complication, the logarithm of the collapsed, 1D power spectrum is smoothed with a 3-point moving average function to produce a smoothed spectrum, as shown in figure 5.2. The noise level of the image is determined by calculating the average value of the smoothed spectrum for frequencies greater than one half of the Nyquist

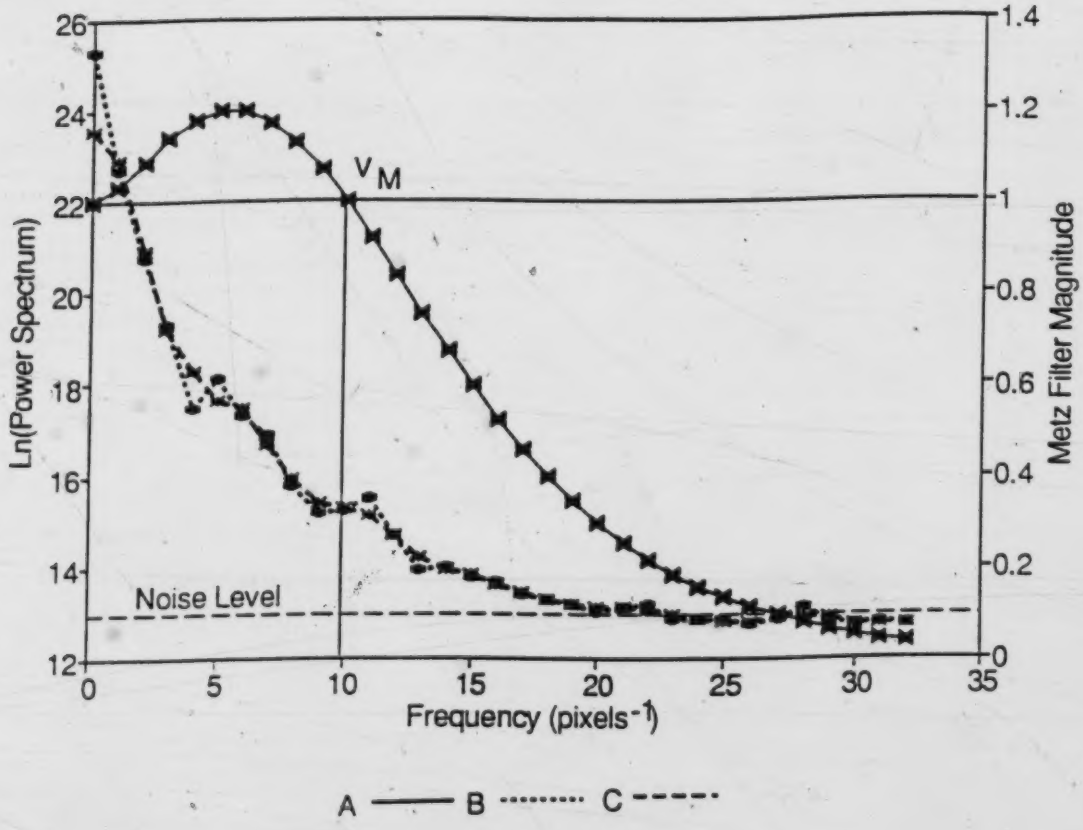

Figure 5.2: The raw (B) and smoothed (C) one dimensional power spectra for a typical SPECT image, and the Metz filter (A) calculated for the image.

frequency (i.e. $\frac{\nu_N}{2}$=16 pixels^{-1} for a 64×64 pixel image). The frequency, ν_M, at which the smoothed spectrum is Ln(10) greater than the noise level is found and the Metz parameter x_M is calculated by solving Eq(5.1.7) using the constraint that the filter equal unity at ν_M. Thus

$$x_M = \frac{\ln[1 - \mathrm{MTF}(\nu_M)]}{\ln[1 - \mathrm{MTF}^2(\nu_M)]}. \tag{5.1.9}$$

The 2D power spectrum is collapsed to 1D by assuming that it is radially symmetric. This amounts to averaging the power spectrum over all frequencies of constant radial distance. Mathematically, the process of collapsing a continuous 2D function to 1D can be expressed as

$$f(r) = \int_0^{2\pi} d\phi \int_0^{\infty} dr' f(x,y)\delta(r - r'), \tag{5.1.10}$$

where $r = (x^2 + y^2)^{1/2}$ and $\phi = \tan^{-1}(\frac{y}{x})$. For discrete functions the collapsing process requires interpolation between the discrete points and Eq(5.1.10) becomes

$$f(mR) = \sum_{i=1}^{N}\sum_{j=1}^{N} W_m^{i,j} f(x_i, y_j), \qquad m = 1, \cdots, N. \tag{5.1.11}$$

where $W_m^{i,j}$ are the interpolation weights and R is the sampling interval. In this work, the weights, $W_m^{i,j}$, were derived using linear interpolation. A collapsed power spectrum is shown in figure 5.2 and provides a good representative of the entire 2D power spectrum from which it is produced. This approximation should be adequate for all situations of clinical interest since, to obtain x_M, it is the noise level of the power spectrum which is sought and not the detailed structure of the power spectrum.

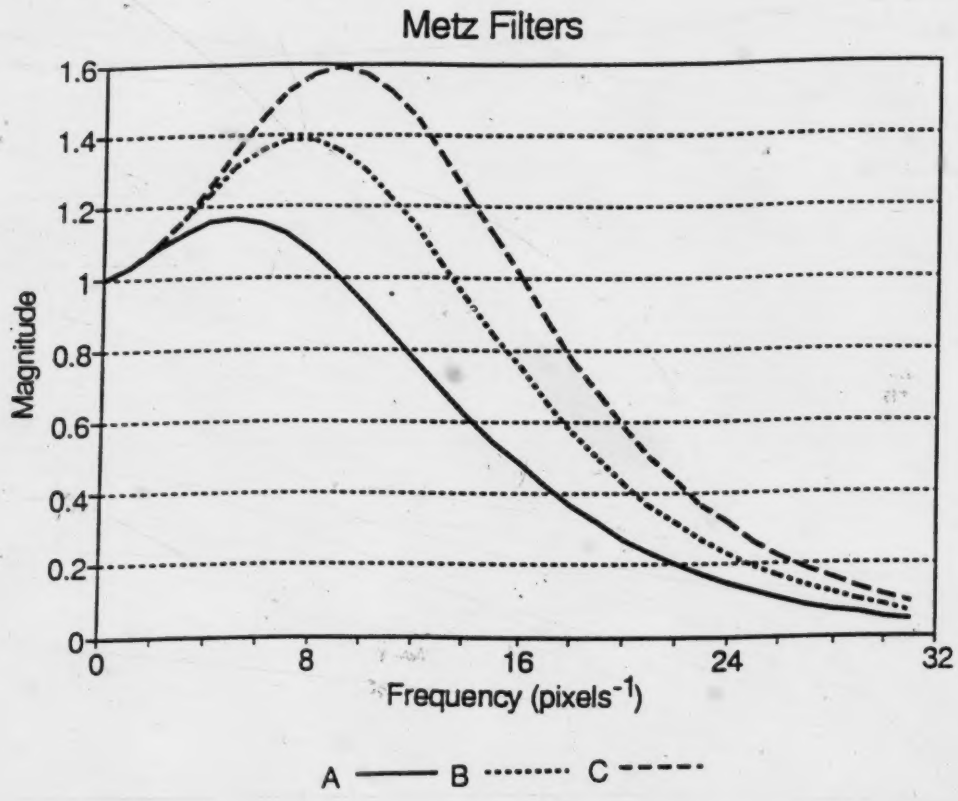

Figure 5.3: Metz filters for (A) $x_M = 2.5$, (B) $x_M = 4.0$, and (C) $x_M = 5.5$, using $P = 1.4$ and $S = 30.0$ to model the MTF.

Some examples of the Metz filter for typical values of the parameter x_M are shown in figure 5.3, using $P = 1.4$ and $S = 30.0$ to model the MTF.

5.2 Scatter and Attenuation

5.2.1 Scatter

In Compton scattering interactions, photons can undergo scattering through an angle of approximately 40 degrees without losing sufficient energy to be rejected by the electronics of the Anger camera. It is quite probable that a photon will

undergo many (up to 6) Compton interactions, each with a small scattering angle and negligible energy transfer, allowing it to be accepted by the electronics. This leads to misplacement of the information (counts) in the projections and in the reconstructed image. The summed effect of the accepted scattered photons (or simply, scatter) on the image is a broad (i.e. low frequency) background which causes the image to appear blurred. It is difficult to compensate for scatter in the reconstruction process since the energy spectrum of each pixel in the projection is unknown. If the energy spectrum for each pixel is available, first principles can be applied to remove much of the scatter [De89, Ha89, Si87]. The majority of camera systems used in clinics today do not provide the energy spectrum information for each pixel.

For these reasons some reconstruction algorithms compensate for scatter by filtering. The Metz filter, described in the previous section, is capable of partially compensating for scatter. This is because the Metz filter is dependent upon the MTF of the system, which includes a scatter component. For low frequencies the Metz filter follows the inverse of the MTF and hence partially deconvolves the scatter component from the image.

Another method for scatter compensation has been proposed in which counts are collected in two energy windows simultaneously, a photopeak energy window and a Compton scatter energy window. From Monte Carlo studies [Fl84] and experiments [Ko90, Fl88] it has been shown that the scatter at each location in the

photopeak projection is correlated to the Compton projection. A certain fraction of the Compton projections, P_C, can be added or subtracted from the corresponding photopeak projections, P_P, to obtain a new set of scatter reduced projections, P',

$$P' = P_P + k \cdot P_C. \tag{5.2.1}$$

This method of scatter reduction, combined with the filtering methods discussed in the previous section, will be discussed in more detail later in this thesis.

5.2.2 Attenuation

Up to this point, the projections obtained by the detector have been assumed to be ray sums of the radioactivity. The more general case is that the projections, $P_\phi(t)$, are partially attenuated, and the Radon Transform function, Eq(4.2.2), must be rewritten as

$$P_\phi(t) = \int\int f(x,y)e^{-g(x,y,\phi)}\delta(x\cos\phi + y\sin\phi - t)dxdy \tag{5.2.2}$$

where $g(x,y,\phi)$ expresses the attenuation of the activity f at the point (x,y) measured at the projection $P_\phi(t)$ and may be expressed as

$$g(x,y,\phi) = \int\int_{s>s_0(x,y,\phi)} \mu(x',y')\delta(-x'\sin\phi + y'\cos\phi - s)dx'dy', \tag{5.2.3}$$

where $\mu(x',y')$ is the linear attenuation coefficient at the point (x',y'), and $s_0(x,y,\phi)$ is given as

$$s_0(x,y,\phi) = -x\sin\phi + y\cos\phi. \tag{5.2.4}$$

To compensate for the loss of activity due to attenuation requires knowing the distribution of attenuation coefficients for the patient. The distribution can be obtained using x-ray CT but generally is not available in the clinical setting. Without the exact distribution of attenuation coefficients approximations must be made to compensate for the attenuation. In most attenuation correction techniques it is assumed that the attenuation coefficient μ is equal to a constant within a defined boundary and is zero outside. In practice the data obtained in the Compton energy window can be used to construct an approximate boundary for the attenuating material, since scattering is largely confined within the material. Using this approximation, Eq(5.2.3) can be rewritten as

$$g(x, y, \phi) = \mu L_\phi(x, y) \tag{5.2.5}$$

where

$$L_\phi(x, y) = \int\int_{s>s_0(x,y,\phi)} \delta(-x' \sin\phi + y' \cos\phi - s) dx' dy'. \qquad \mu \neq 0. \tag{5.2.6}$$

$L_\phi(x, y)$ is called the attenuation length for the point (x, y) for a given angle ϕ, and represents the distance from the point (x, y) to the edge, or through, the attenuating material (i.e. $\mu \neq 0$) along the ray defined by t and ϕ in the positive s-direction. The attenuation lengths are shown in figure 5.4.

There are three common attenuation methods which are used in conjunction with traditional filtered backprojection reconstruction. All of the methods assume that the boundary of the attenuating material is known, and that the attenuation

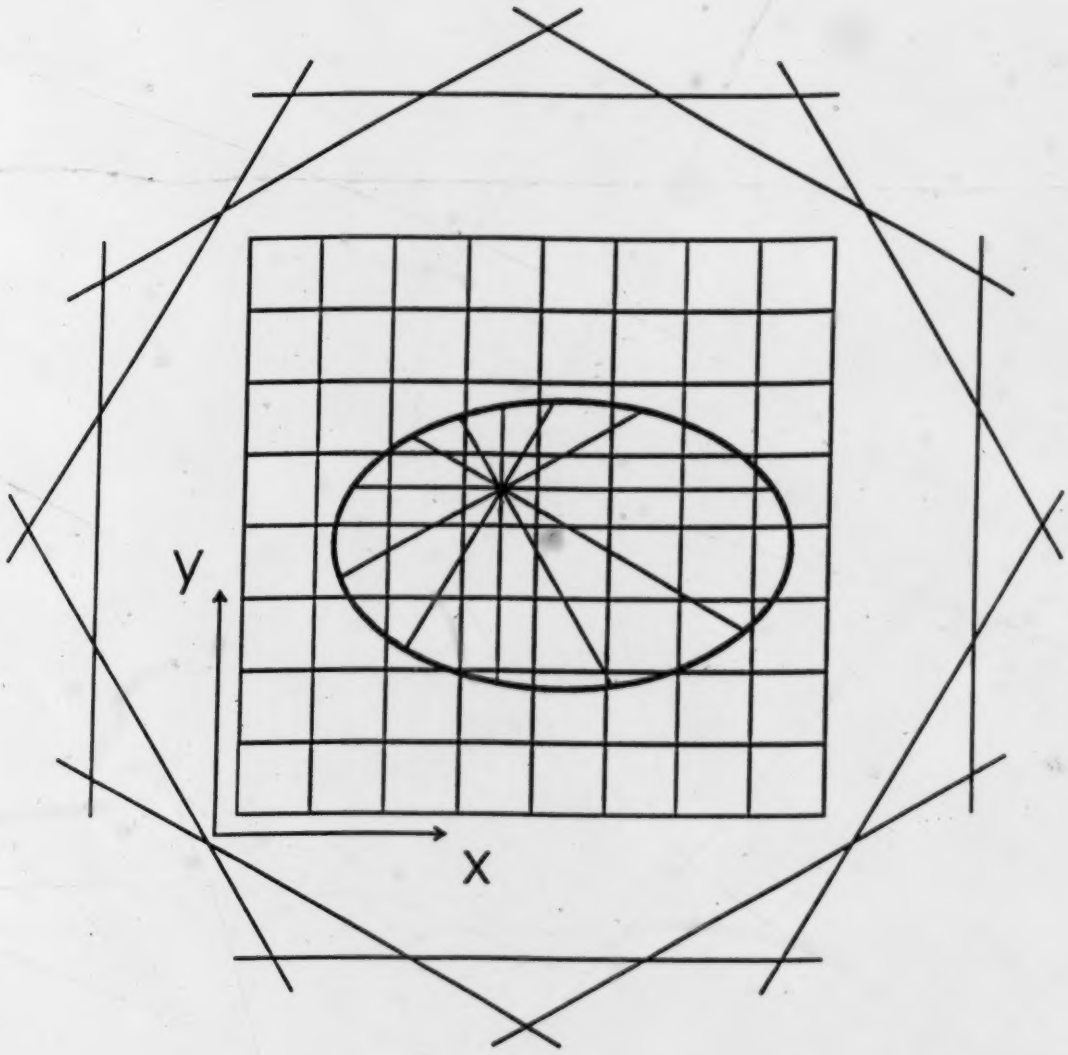

Figure 5.4: Attenuation lengths $L_\phi(x, y)$ for an arbitrary reconstruction cell at (x,y).

coefficient is a constant within that boundary and zero outside. The difference between the methods is the point in the reconstruction where each is applied. They are termed pre-processing, intrinsic, and post-processing attenuation correction.

In pre-processing attenuation correction, opposing projections are summed and scaled based on their combined attenuation lengths $\mathcal{L}_\phi(t)$ to obtain a set of attenuation corrected projections (see figure 5.5) [Bu79]. This method of attenuation correction assumes that both the activity and the attenuation coefficient be a constant within the attenuation boundary. The set of attenuation corrected projections are given by

$$P'_\phi(t) = \mu\mathcal{L}_\phi(t)\frac{P_\phi(t) + P_{\phi+\pi}(-t)}{4e^{-\mu\mathcal{L}_\phi(t)/2}\sinh(\mu\mathcal{L}_\phi(t)/2)}. \tag{5.2.7}$$

The attenuation length $\mathcal{L}_\phi(t)$ can be obtained from the previously mentioned attenuation lengths $L_\phi(x,y)$ using

$$\mathcal{L}_\phi(t) = L_\phi(x,y) + L_{\phi+\pi}(x,y) \tag{5.2.8}$$

provided the constraint

$$t = x\cos\phi + y\sin\phi \tag{5.2.9}$$

is satisfied by x and y.

The post-processing method involves correcting each point in the reconstructed image based on an average attenuation coefficient. This method is commonly referred to as Chang's attenuation correction method [Ch78] and may require iterative techniques to determine the attenuation correction coefficients. The method assumes the linear attenuation coefficient $\mu(x,y)$ is constant inside the medium and

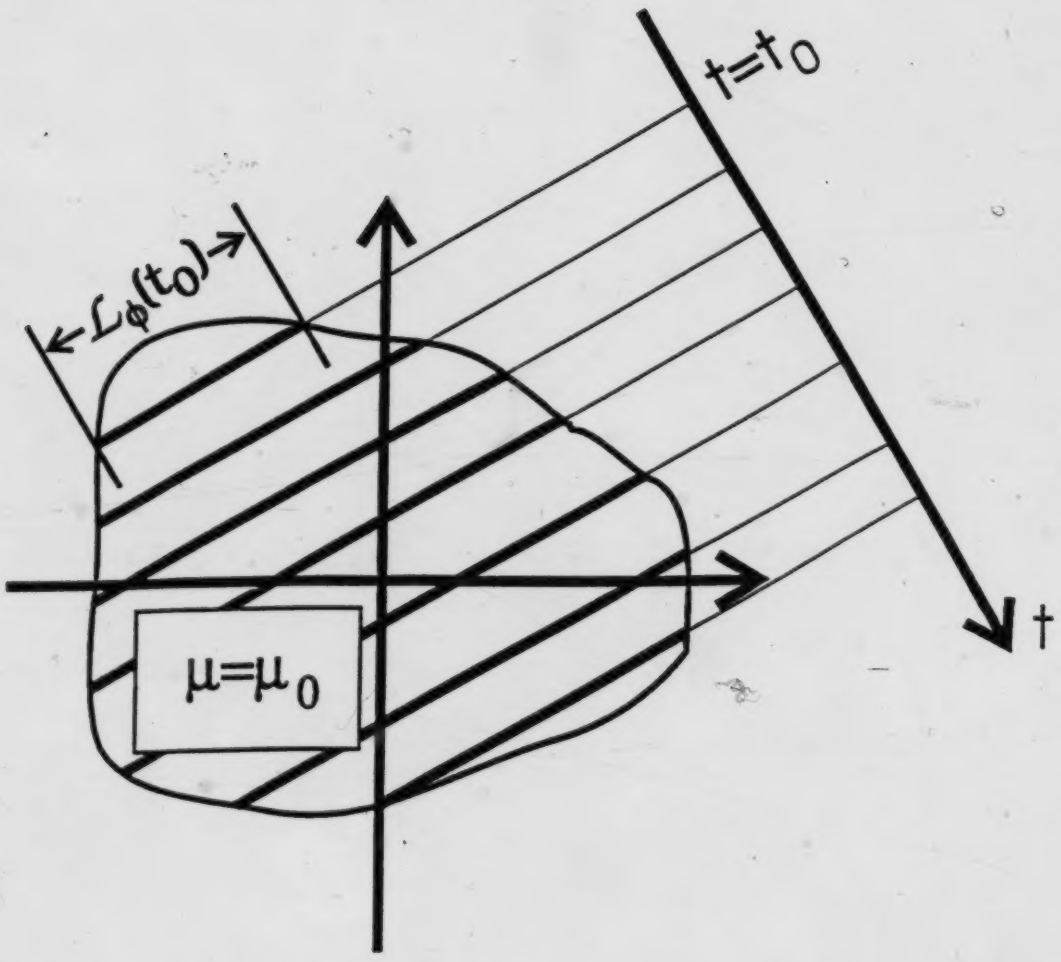

Figure 5.5: Pre-processing attenuation lengths, $\mathcal{L}_\phi(t)$.

zero outside. In this approximation, correction for attenuation reduces to calculating an average correction coefficient for each point in the image. The coefficients are given as

$$c(x_0, y_0) = \frac{1}{\frac{1}{2\pi}\int_0^{2\pi} e^{-\mu L_\phi(x_0,y_0)} d\phi} \approx \frac{1}{\frac{1}{M}\sum_{i=1}^{M} e^{-\mu L_{\phi_i}(x_0,y_0)}}, \qquad (5.2.10)$$

where $L_{\bar{\phi}}(x_0, y_0)$ is shown in figure 5.6. Each point in the original reconstructed image, I, is multiplied by a correction coefficient to obtain a attenuation-corrected image, I'. The correction coefficients may be further refined using an iterative procedure. Firstly, I' is forward projected (as discussed in Section 5.3) to obtain a new set of projections, P'_ϕ. These new projections are subtracted from the original projections, P_ϕ, to obtain a set of error projections, P_ϕ^{Error}. The error projections are back-projected to obtain an error image, I^{Error}. The error is multiplied by the previously determined correction coefficients and added to I' to obtain an improved image I''. This procedure can be repeated, iteratively, until the average pixel count in the error image reaches some predefined tolerance.

The intrinsic correction method involves filtering with an attenuation dependent filter and back-projecting with an exponential back projector [Gu81]. This type of attenuation correction is computer intensive and seldomly used clinically, and will not be discussed in this work.

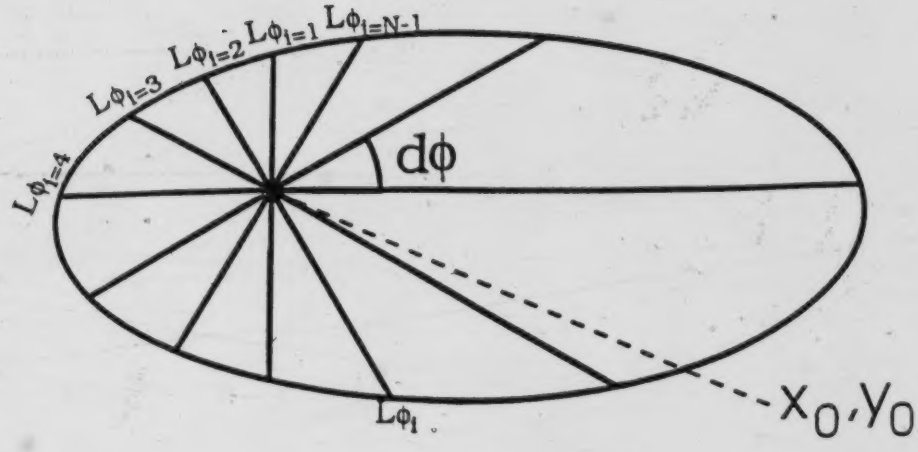

Figure 5.6: Post-processing attenuation lengths, $L_\phi(x_0, y_0)$.

5.3 Discrete Projections and Transforms

The projections obtained in practice are not continuous but sampled over discrete spatial intervals. To implement the above mathematics, using a computer, requires that the equations be made spatially-discrete. The projection at an angle ϕ become

$$P_\phi(t) \rightarrow P_\phi(mT) \text{ for } m = -\frac{N}{2}, \cdots, 0, \cdots, \frac{N}{2} - 1 \tag{5.3.1}$$

where T is the sampling interval. Employing the discrete FT, Eq(4.2.13) becomes

$$S_\phi(\omega) \rightarrow S_\phi(m\frac{2W}{N}) = \frac{1}{2W} \sum_{k=-\frac{N}{2}}^{\frac{N}{2}-1} P_\phi(\frac{k}{2W}) e^{-i2\pi\frac{mk}{N}}, \tag{5.3.2}$$

where $W = \frac{1}{2T}$ is the sampling interval in Fourier space. In the same manner Eq(4.2.19) and Eq(4.2.20) must be rewritten as

$$f(x,y) = \frac{\pi}{k} \sum_{i=1}^{k} Q_{\phi_i}(x\cos\phi_i + y\sin\phi_i) \tag{5.3.3}$$

and

$$Q_\phi(t) \rightarrow Q_\phi(\frac{k}{2W}) = \frac{2W}{N} \sum_{k=-\frac{N}{2}}^{\frac{N}{2}-1} S_\phi(m\frac{2W}{N}) |m\frac{2W}{N}| e^{i2\pi\frac{mk}{n}} \tag{5.3.4}$$

where the k angles, ϕ_i, are those for which the $P_{\phi_i}(t)$'s are known.

The distribution $f(x,y)$ is also not continuous but is made spatially-discrete to lie within a reconstruction grid such that $f(x,y)$ becomes $f(x_i,y_j)$ where $i,j = 1,\cdots,N$. The finite extents of the projection sampling and reconstruction grid require that Eq(5.3.3) be modified to incorporate this in the backprojection, since the argument of Q_{ϕ_i} may not coincide with that of a known Q_{ϕ_i}. Therefore, some type of interpolation will be required during reconstruction. The simplest solution

to this problem would be to calculate the value of the argument $x_i \cos\phi_k + y_j \sin\phi_k$ and determine the nearest neighbors to this value. Based on the differences between the actual value and the neighbors', linear interpolation could be employed. This interpolation method of backprojection is demonstrated in figure 5.7 and can be expressed, mathematically, by rewriting Eq (5.3.3) as

$$f(x_i, y_j) = \frac{\pi}{k} \sum_{m=1}^{N} \sum_{l=1}^{k} W_{i,j}^{l,m} Q_{\phi_l}(mT), \tag{5.3.5}$$

where many of the weights, $W_{i,j}^{l,m}$, are zero and T is the projection bin's sampling width.

The inverse problem of obtaining the projections from a distribution when both are spatially discrete also requires interpolation methods. The process of determining the discrete projections from a discrete reconstruction grid is termed forward projection. Mathematically, the forward projection process can be expressed as

$$P_{\phi_l}(mT) = \sum_{i=1}^{N} \sum_{j=1}^{N} W_{l,m}^{i,j} f(x_i, y_j), \qquad l, m = 0, \cdots, N \tag{5.3.6}$$

where many of the weights, $W_{l,m}^{i,j}$, are zero. Equation (5.3.6) is simply the digitization of Eq(4.2.2), the Radon transform. Likewise, if the distribution lies within an attenuating material then the attenuated Radon transform, Eq(5.2.2), becomes

$$P_{\phi_l}(mT) = \sum_{i=1}^{N} \sum_{j=1}^{N} W_{l,m}^{i,j} \exp^{(-\mu L_{\phi_l}(x_i, y_j))} f(x_i, y_j), \qquad l, m = 0, \cdots, N. \tag{5.3.7}$$

The backprojection and forward projection weights, $W_{i,j}^{l,m}$ and $W_{l,m}^{i,j}$, may be calculated using various interpolation methods. Two of the most common techniques, linear interpolation and area interpolation, will be discussed in detail.

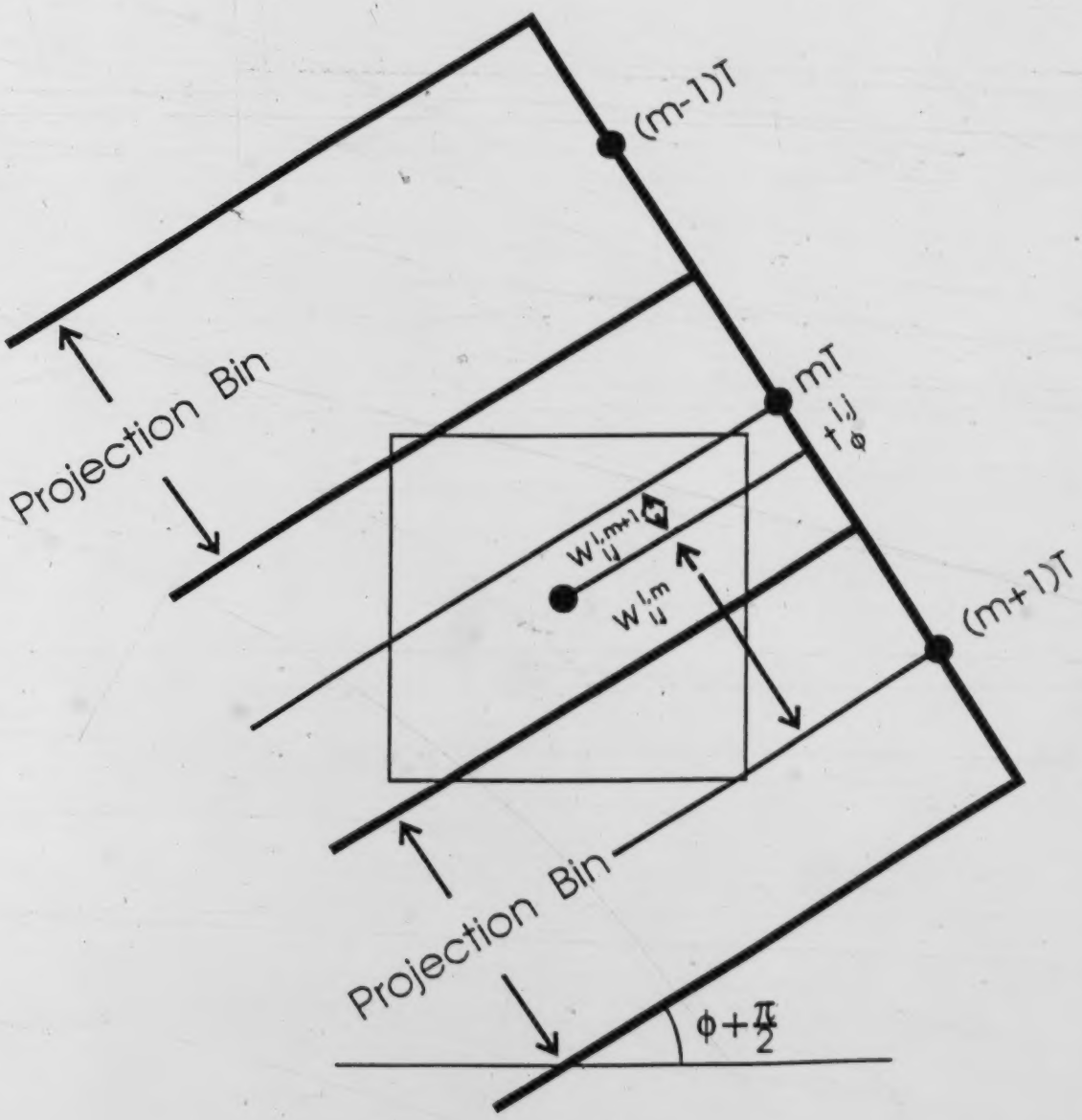

Figure 5.7: The geometry for the linear interpolation weighting.

5.3.1 Linear Interpolation Weighting

In linear interpolation weighting all the information in each reconstruction image pixel (x_i, y_j) and in the projection bins $P_\phi(mT)$ is assumed to be concentrated at the center of each pixel. The general geometry of this problem is illustrated in figure 5.7.

For a given projection angle ϕ the coordinate $t_\phi^{i,j}$ for the reconstruction cell (x_i, y_j) can be calculated according to

$$t_\phi^{i,j} = x_i \cos\phi + y_i \sin\phi. \tag{5.3.8}$$

In general $t_\phi^{i,j}$ is not one of the sampled projection points but lies between two of the sampled points $t = mT$ and $t = (m+1)T$, where T is the sampling interval (width of the bin) of the projection. For the backprojection step of the reconstruction the weights $W_{i,j}^{l,\alpha}$ in Eq(5.3.5) are all zero, for a given i, j and l, except for $\alpha = m$ and $\alpha = m+1$ which are given by

$$W_{i,j}^{l,m} = \frac{(m+1)T - t_\phi^{i,j}}{T} \tag{5.3.9}$$

$$W_{i,j}^{l,m+1} = \frac{t_\phi^{i,j} - mT}{T} = 1 - W_{i,j}^{l,m}. \tag{5.3.10}$$

Likewise, in the forward projection step of the reconstruction the weights $W_{l,\alpha}^{i,j}$ are all zero, for a given i, j and l, except for $\alpha = m$ and $\alpha = m+1$ which are given as

$$W_{l,m}^{i,j} = \frac{(m+1)T - t_\phi^{i,j}}{T} \tag{5.3.11}$$

$$W_{l,m+1}^{i,j} = \frac{t_\phi^{i,j} - mT}{T} = 1 - W_{i,j}^{l,m}, \tag{5.3.12}$$

and are identical to their back-projection counterparts.

5.3.2 Area Interpolation Weighting

In area interpolation weighting all the information in each reconstruction image pixel (x_i, y_j) and in the projection bins $P_\phi(mT)$ is assumed to be uniformly distributed over each pixel. This area interpolation method is dependent upon the area demarcated by the intersection of a projection bin strip with a given reconstruction cell.

The geometry of this problem, shown in figure 5.8, is such that a maximum of three projection bins are connected to a given reconstruction cell. The weights $W_{i,j}^{l,m}$ and $W_{l,m}^{i,j}$ are directly proportional to the area formed by the intersection of the strip of projection bin $P_{\phi_l}(mT)$ and the reconstruction cell at (x_i, y_j). The cells of the reconstruction grid are square and project different lengths onto the t-axis (i.e. the projection axis) for different projection angles. The length of the projection of the cell's area onto the projection axis is characterized by the values t_- and t_+, as shown in figure 5.9, and determines how many and which projections bins are connected to the cell, for a given projection angle ϕ. It is only necessary to consider the weights in the first half quadrant since extension to the other quadrants requires only simple symmetry transforms. In figure 5.9 the most general case is shown in which three projection bins are connect to the cell. To determine the weights for the three projection bins, each corner point on the square cell, (a, b, c, d), is projected onto the t-axis to determine the corresponding t-coordinate, (t_a, t_b, t_c, t_d), as shown in figure 5.9. Since the bin coordinate marks the center of the bin, its edges can be

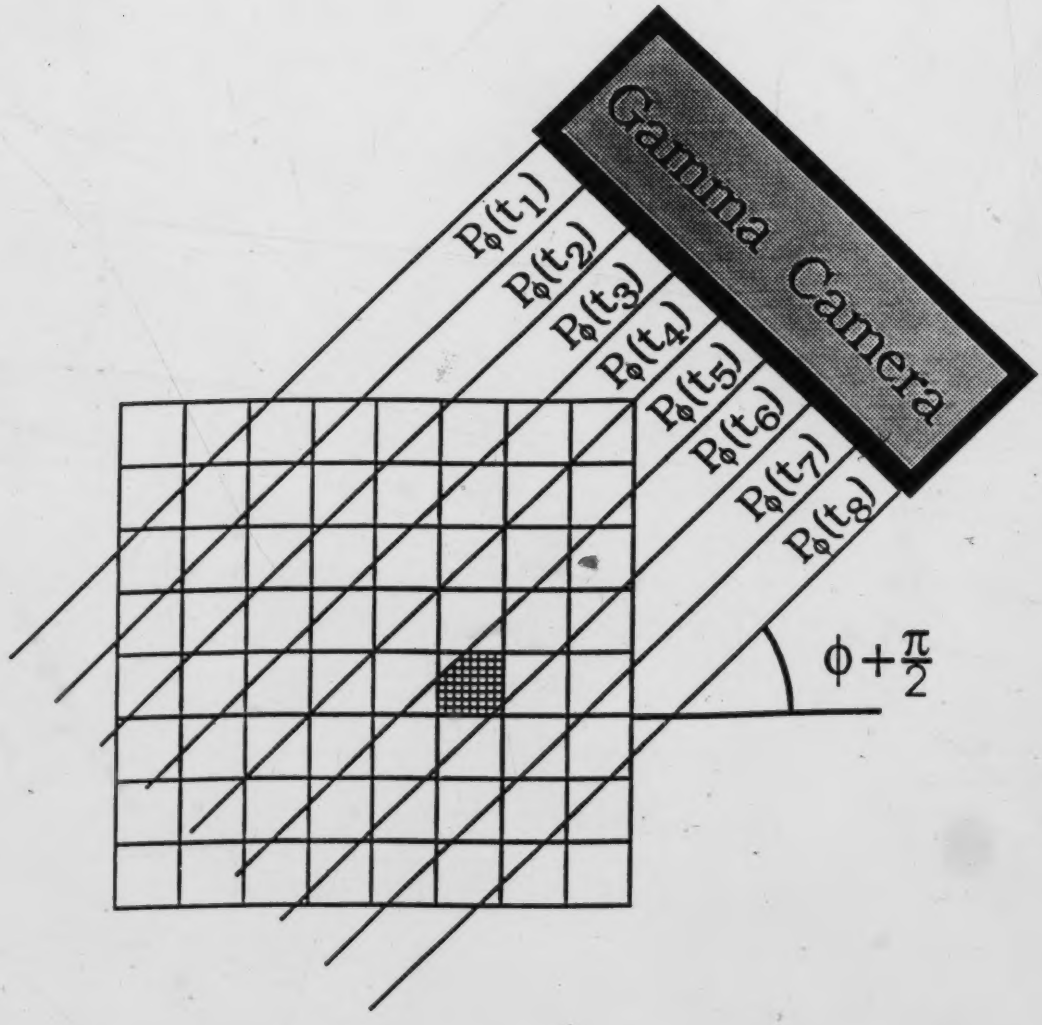

Figure 5.8: The geometry for the area interpolation weighting.

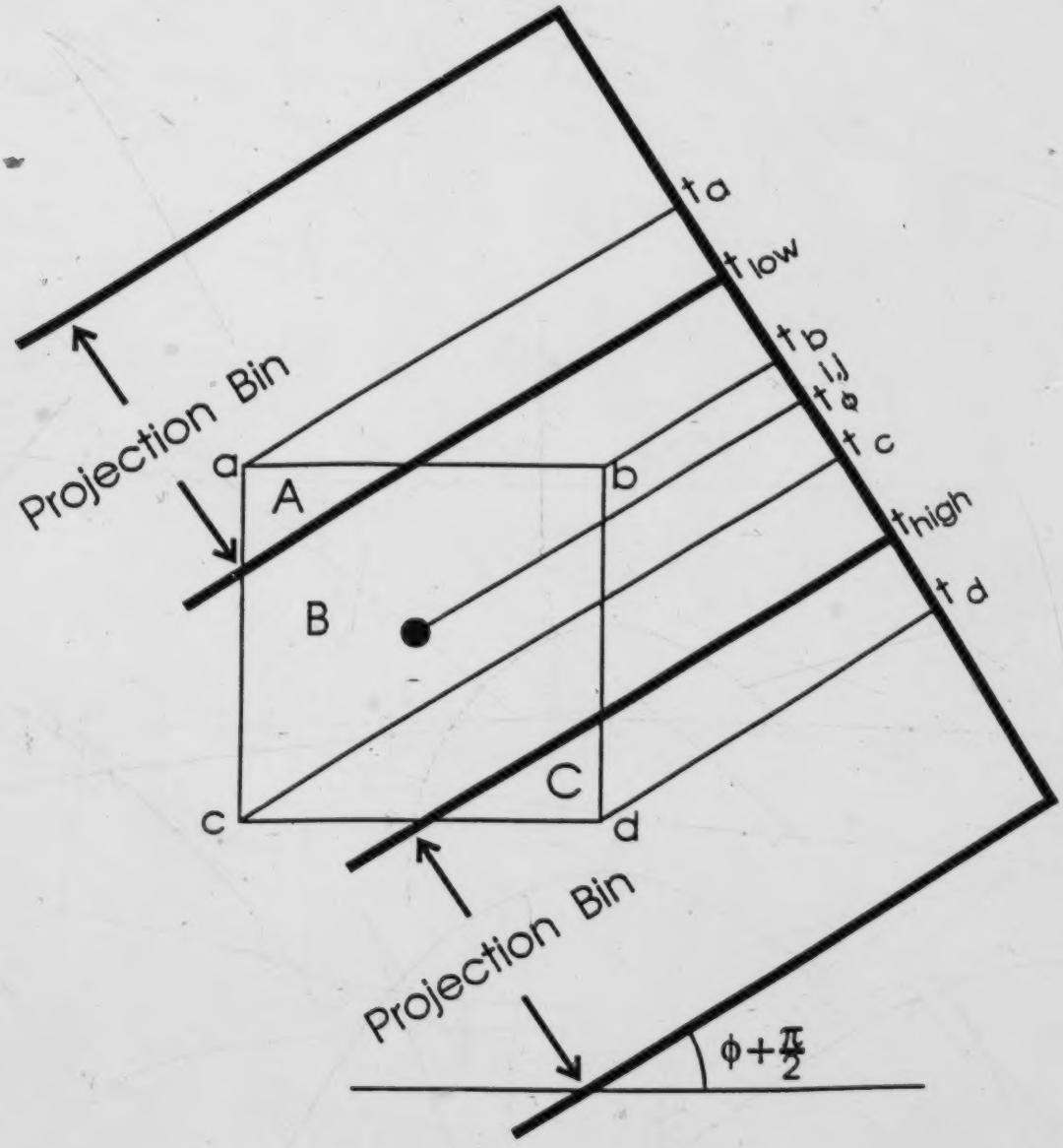

Figure 5.9: Blow-up of one reconstruction cell for the area interpolation weighting.

readily calculated. These are labelled t_{low} and t_{high} in figure 5.9. Having determined the six values $t_{a,b,c,d,\text{low},\text{high}}$, weights can be determined using simple geometric and trigonometric principles.

The total area of the cell is unity, measured in units of T, which imposes the constraint that the sum of the weights equal one and therefore only two of the three weights need to be calculated. With reference to figure 5.9, consider area A for $\phi \leq \frac{\pi}{4}$. There are three cases to attend to: $(t_{\text{low}} > t_b)$, $(t_a \leq t_{\text{low}} \leq t_b)$ and otherwise. For the case $(t_{\text{low}} > t_b)$ the area A is divided into two parts, A_1 and A_2. Mathematically these areas (in units of T^2) are given by

$$A_1 = \frac{1}{2}\tan\phi \tag{5.3.13}$$

$$A_2 = \frac{\frac{t_{\text{low}} - t_b}{T}}{|\cos\phi|}. \tag{5.3.14}$$

For the case when $(t_a \leq t_{\text{low}} \leq t_b)$ the area A (in units of T^2) is

$$A = \frac{1}{2}\frac{\frac{t_{\text{low}} - t_a}{T}}{|\cos\phi \sin\phi|}. \tag{5.3.15}$$

For all other cases the area A is zero. Likewise, for area C for $\phi \leq \frac{\pi}{4}$, there are three cases to consider: $(t_{\text{high}} < t_c)$, $(t_c \leq t_{\text{high}} \leq t_d)$ and otherwise. For the case $(t_{\text{high}} < t_c)$ the area C is subdivided into two areas, C_1 and C_2. These areas (in units of T^2) are given as

$$C_1 = \frac{1}{2}\tan\phi \tag{5.3.16}$$

$$C_2 = \frac{\frac{t_c - t_{\text{high}}}{T}}{|\cos\phi|}. \tag{5.3.17}$$

For the case ($t_c \leq t_{high} \leq t_d$) the area C (in units of T^2) is given by

$$C = \frac{1}{2} \frac{\frac{t_d - t_{high}}{T}}{|\cos\phi \sin\phi|}. \tag{5.3.18}$$

The last area B is simply

$$B = 1 - (A + C) \tag{5.3.19}$$

Having determined the three areas, (A, B, C), in units of T^2 the weights are numerically equal to the value of the areas (neglecting dimensionality) and are given as

$$W_{i,j}^{l,m-1} = W_{l,m-1}^{i,j} = A \tag{5.3.20}$$

$$W_{i,j}^{l,m} = W_{l,m}^{i,j} = B \tag{5.3.21}$$

$$W_{i,j}^{l,m+1} = W_{l,m+1}^{i,j} = C \tag{5.3.22}$$

5.3.3 Iterative Correction to Weighting

In practice, the projections obtained from the forward projection of the reconstruction grid do not reproduce the reconstruction grid upon back projection. This is due to the finite number of projections and the fact that the projections and the reconstruction grid are spatially discrete. To obtain projections, through the forward projection of the reconstruction grid, that upon back projection reproduce the reconstruction grid, iterative techniques must be used [Ka88b]. This is true for both the linear and the area interpolation methods.

The basic outline of the iterative technique is as follows; 1) the original image is forward projected to obtain the first approximation to the projections, 2) these

projections are backprojected to obtain the first approximation to the original image, 3) the approximated image is subtracted from the original to obtain an error image which is forward projected to obtain error projections, 4) the error projections are added to the first approximation of the projections, which produces an improved, second approximation to the projections. The process continues iteratively until the average pixel value for the error projections reaches some predefined tolerance. In this way a set of projections can be obtained which, upon backprojection, accurately reproduce the original image. Attenuation effects are incorporated into this iterative procedure if the original image has been corrected for attenuation.

5.4 Image Comparison Techniques

To quantitatively assess the performance of a given reconstruction method or image processing technique, it is necessary to compare the reconstructed or the processed images, $S_{i,j}$, to a reference image, $R_{i,j}$, which is assumed to be a true representation of the actual distribution of radioactivity. $S_{i,j}$ can be compared to $R_{i,j}$ using a variety of image evaluation techniques. To obtain an overall comparison of the processed image with the reference image a ψ-comparison value is calculated according to

$$\psi = \sum_{i,j} \frac{(R_{i,j} - f \cdot S_{i,j})^2}{R_{i,j}}, \tag{5.4.1}$$

where f is a scaling factor chosen to minimize ψ. For a given $S_{i,j}$ and $R_{i,j}$

$$\frac{\partial \psi}{\partial f} = 0 \quad \Rightarrow \quad f_\psi = \frac{\sum_{i,j} S_{i,j}}{\sum_{i,j} \frac{(S_{i,j})^2}{R_{i,j}}}. \tag{5.4.2}$$

The scaling factor f is required since the count levels of $S_{i,j}$ and $R_{i,j}$ may differ greatly. The larger the ψ-value, the more poorly $S_{i,j}$ compares to $R_{i,j}$. A series of images, $\{S^k_{i,j}\}$, can be compared to a single reference image $R_{i,j}$, by calculating an improvement index Ψ^m_k as

$$\Psi^m_k = \frac{\psi_m - \psi_k}{\psi_m}. \tag{5.4.3}$$

Ψ^m_k represents the fractional improvement of the image $S^k_{i,j}$ over image $S^m_{i,j}$ with respect to comparison to $R_{i,j}$. A positive fractional improvement value implies that $S^k_{i,j}$ is a better representation of $R_{i,j}$ than $S^m_{i,j}$, by the fractional amount. Negative fractional values imply that $S^k_{i,j}$ is a poorer representation of $R_{i,j}$ than $S^m_{i,j}$, by the fractional amount (which may be less than -1.0). In most cases the improvement index Ψ^m_k will be presented rather than the actual value of ψ for $S^k_{i,j}$.

Chapter 6

Experiments

Two sets of experiments were performed to investigate the merits of certain components of the traditional filtered back-projection method of reconstruction. In the first set of experiments, the reduction of scatter in planar images (projections), using Compton window subtraction in conjunction with a Butterworth filter or an image dependent Metz filter, was investigated. The second set of experiments was used to study two attenuation correction methods used in SPECT.

6.1 Takahashi Phantom Study - Scatter Reduction/Compensation

6.1.1 Experiments

A set of experiments were carried out to investigate the performance of scatter reduction techniques using a specially designed phantom, hereafter called the Takahashi Phantom [Ta89], which is shown in figure 6.1. The experimental set-up is shown in figure 6.2. A low energy, general purpose, parallel hole collimator was used and the collimator to source distance was fixed at 13.0cm for all images. The phantom was imaged for three thicknesses of scatter material (0cm, 5.6cm, and 11.9cm), interposed between the camera's collimator and the phantom. Two sealed Plexiglass

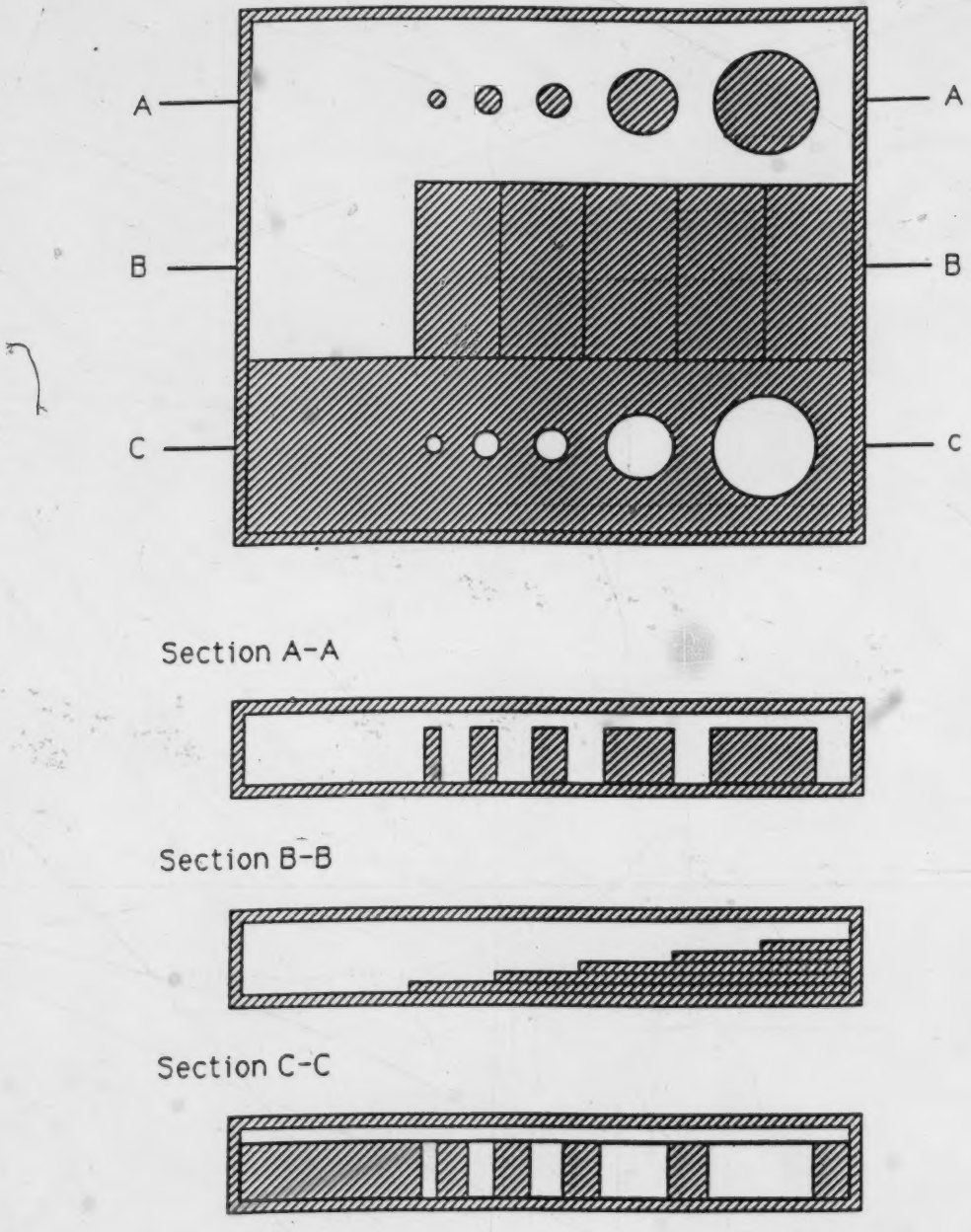

Figure 6.1: Schematic diagram of the Takahashi phantom. Reproduced with Author's permission [Ta89].

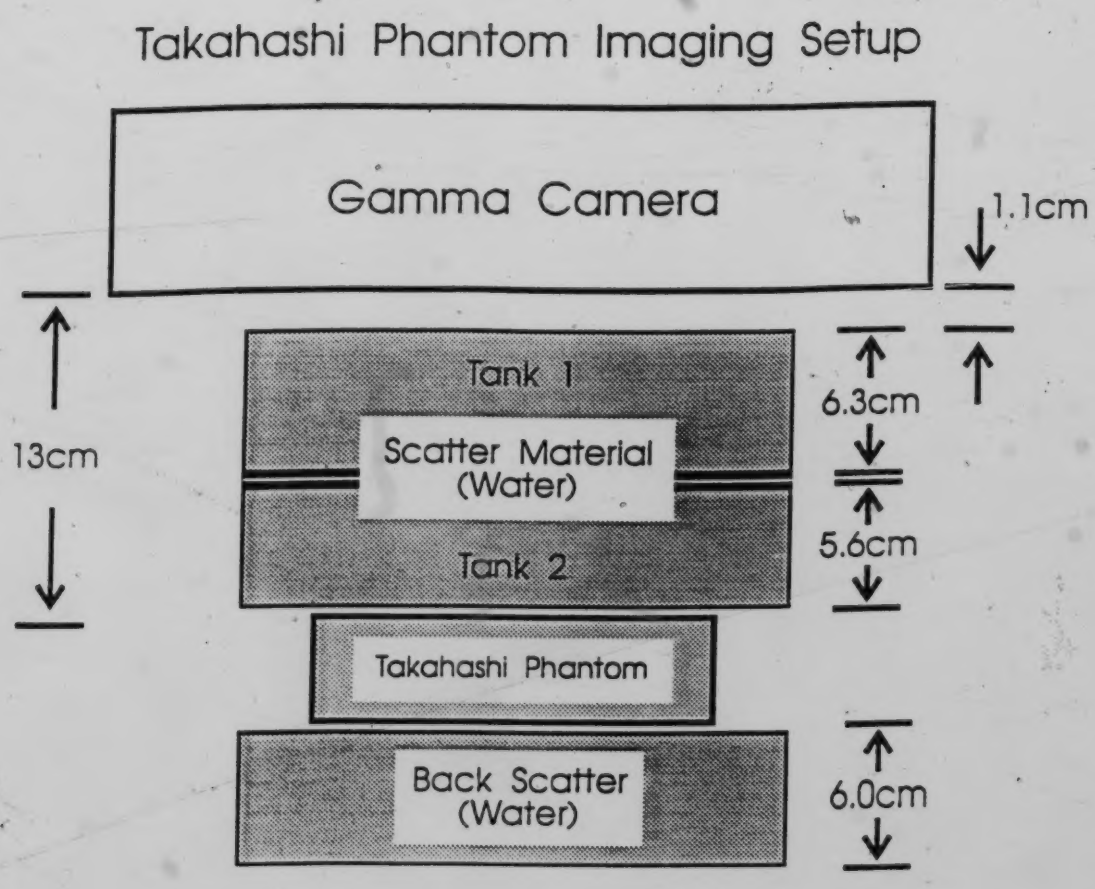

Figure 6.2: The experimental set-up for the Takahashi phantom experiment.

flood tanks (one 5.6 cm thick and the other 6.3 cm thick) filled with water were used for scatter material. A sealed Plexiglass flood tank (6 cm thick) filled with water was used for backscatter and was present for all images. The planar images (projections) of the phantom were collected into two energy windows simultaneously; a photopeak window (129-151keV) and a Compton window (106-128keV). The sum of counts, in the two energy windows, for a given depth of scatter material, was either 0.5 million or 5.0 million counts. All images were collected into matrices of size 128×128 pixels. The images obtained from these experiments are listed in Table 6.1.

Using the same collimator as above, a very high count, high spatial resolution, reference image was obtained by placing the phantom directly on the collimator and acquiring approximately 73 million counts in the photopeak window into a matrix of size 128×128 pixels. The backscatter tank was present during the collection of the reference image so that the positioning of the phantom was not disturbed. The reference image was used as a *gold standard* for comparison of images modified using various image processing techniques, as described below.

6.1.2 Image Processing Methods

The images obtained in the experiments were collapsed from 128×128 pixels to 64×64 pixels and processed using Compton window subtraction in conjunction with either a Metz or a Butterworth filter.

For each set of images in Table 6.1, such as Image 1a and Image 1b, a fraction k

Takahashi Phantom Experiment					
Name	Energy Window	Scatter Depth	Counts		
			Max	Ave	Total
Low Count Images					
Image 1a	Compton	0.0 cm	103	32	1.31E5
Image 1b	Photopeak	0.0 cm	255	90	3.68E5
Image 2a	Compton	5.6 cm	126	44	1.80E5
Image 2b	Photopeak	5.6 cm	221	78	3.20E5
Image 3a	Compton	11.9 cm	139	48	1.97E5
Image 3b	Photopeak	11.9 cm	208	74	3.03E5
High Count Images					
Image 4a	Compton	0.0 cm	868	321	1.31E6
Image 4b	Photopeak	0.0 cm	2310	900	3.68E6
Image 5a	Compton	5.6 cm	1089	438	1.80E6
Image 5b	Photopeak	5.6 cm	2014	782	3.20E6
Image 6a	Compton	11.9 cm	1141	482	1.97E6
Image 6b	Photopeak	11.9 cm	1846	738	3.03E6
Reference Image					
Image Ref	Photopeak	0.0 cm	17608	6584	2.70E7

Table 6.1: Planar images (projections) obtained from the Takahashi phantom experiments.

of the data from the Compton image was added to or subtracted from the photopeak image to produce a combined image. The value of k ranged from -1 (i.e. subtraction) to $+1$ (i.e. addition) in steps of 0.1. For each value of k, the combined image was filtered using one of three different filters: (1) a Metz filter with a constant $x_M = 4.3$; (2) a Metz filter with a variable x_M (i.e. x_M was calculated based on the power spectrum of the image); and (3) a Butterworth filter with $x_B = 12.5$. The parameters $P = 1.4$ and $S = 30.0$ were used to model the MTF of the system for the Metz filters, as discussed in Section 5.1. Previous studies of the MTF have shown these values to be best for typical imaging situations using this system. Each of the 63 combined images (i.e. 3 filtering methods and 21 values of k) were compared to the reference image, and an improvement index (with respect to Image 1b filtered with a Metz filter with $x_M = 4.3$) was calculated. The above process was repeated for all 6 data sets listed in Table 6.1. For each data set the improvement index was calculated with respect to the photopeak data filtered with a Metz filter with $x_M = 4.3$.

The reference image was not processed with any filters as the average pixel count in the reference image was very high and therefore such be a very good representation of the actual distribution of radioactivity in the phantom.

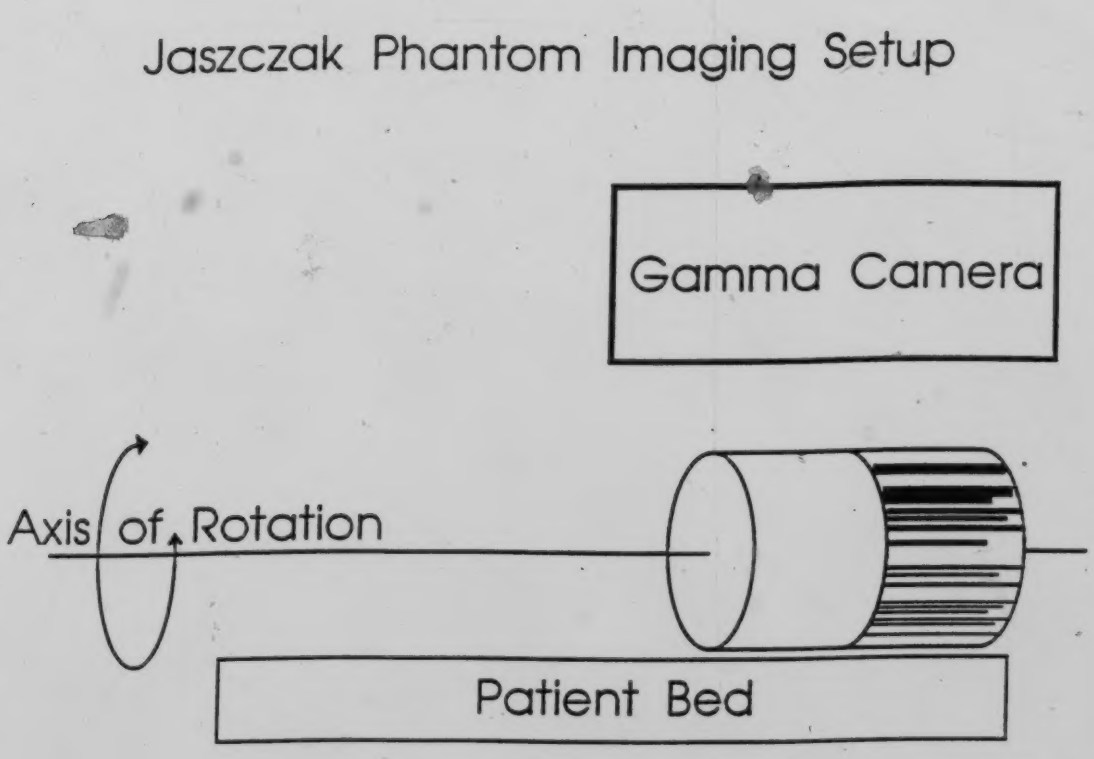

Figure 6.3: The experimental set-up for the Jaszczak phantom experiment.

6.2 Jaszczak Phantom Study - Attenuation Correction

6.2.1 Experiment

Pre and post-attenuation correction algorithms were studied using a commercial SPECT phantom known as the Jaszczak phantom. The experimental set-up is shown in figure 6.3. Sixty-four projection images of the phantom were taken at equal angular intervals as the camera rotated through 360 degrees in an elliptical orbit. A 64×64 pixel image was acquired at each projection angle for both a

photopeak energy window (129 - 151 keV) and a Compton energy window (106 - 128 keV). Approximately 1.1 million counts were detected at each projection angle (i.e. $\approx$ 780 kcounts in the photopeak and $\approx$ 350 kcounts in the Compton). Care was taken to ensure that the axis of the cylindrical phantom was parallel to the axis of rotation of the camera.

A reference image was obtained by placing the bottom surface of the phantom against the collimator of the camera. Using only the photopeak energy window, a 24 million count image was acquired into a 256×256 pixel matrix. This reference image was used as a template for analyzing reconstructed transaxial slices lying in the bottom half of the phantom; the 256×256 pixel matrix was used to simplify the alignment of this image with the reconstructed transaxial slices.

6.2.2 Image Processing Methods

The raw set of projections obtained from the experiment was transformed to produce two sets of filtered projections. The first set of filtered projections was obtained by subtracting one-half of the data in each Compton projection from its corresponding photopeak projection to produce a set of scatter reduced projections. The scatter reduced projections were filtered using a Butterworth filter with $x_B = 12.5$ and $\nu_c = 15.36$ pixels^{-1}. A second set of projections were produced by filtering each photopeak projection with a Metz filter constructed from the parameters $P = 1.4$, $S = 30.0$, and a constant $x_M = 4.3$. Each set of filtered data was used to reconstruct a transaxial slice of the phantom, which in turn was used to define the phantom

boundary. The reference image was aligned, such that its boundary coincided with the defined boundary, and collapsed to a 64×64 pixels matrix. This allowed the reference and reconstructed images to be aligned with an accuracy of one-quarter of a pixel.

The attenuation coefficient, μ, was chosen to be 0.14cm^{-1} within the boundary and zero outside the boundary. The value of 0.14cm^{-1} is slightly less than the narrow beam geometry value of 0.15cm^{-1}, for 140keV photons in water.

The boundary obtained from the attenuated transaxial slice was used to determine the attenuation lengths, for either the pre-processing or the post-processing attenuation correction methods, as described in Section 5.2.2. For the post-processing attenuation correction method, a correction matrix was produced according to Eq(5.2.10). For the pre-processing attenuation correction method, the projections were corrected for attenuation according to Eq(5.2.7).

The filtered projection data were used to reconstruct the same transaxial slice of the phantom, this time accounting for attenuation by employing either the pre-processing or the post-processing attenuation correction method. The four images obtained (two filtering methods combined with two attenuation correction methods) were compared to the reference image and an improvement index was calculated for each.

Next, using only the Metz filtered projections, the effects of an incorrect attenuation boundary were evaluated for each of the two attenuation correction meth-

ods. The boundary was either shifted or distorted by a defined amount, and a new transaxial slice was reconstructed, using each attenuation correction method. The boundary was distorted (enlarged) by increasing one of the ellipse's axes while keeping the other fixed. The reconstructed slices obtained were compared to the reference image and an improvement index, with respect to the exact boundary case, was calculated. The procedure was repeated for shifts of 1 to 5 pixels and distortions of 1 to 6 pixels.

Iterations in the post-processing attenuation correction method and the forward projection step, as described in Section 5.2.2, were employed for the exact, the shifted, and the distorted boundary cases, to determine if improvements could be gained through the iterative procedure. For each iteration in the attenuation correction, a certain number of iterations were also performed in the forward projection step. In addition, two interpolation methods, linear and area, were used in the reconstruction process to determine which method produced the most accurate transaxial slice. Each reconstructed slice, for the different boundaries and interpolation methods, was evaluated in two ways. The reconstructed slice was compared with the reference image and an improvement index was calculated. A one-dimensional profile of the reconstructed slice was obtained by summing the slice over one-dimension (i.e. obtaining a projection of the slice). The obtained profile was plotted with the profile for the exact boundary to determine if asymmetries or distortions were introduced by the attenuation correction methods.

6.3 Computer Simulation Experiment

A computer simulation was performed to further investigate the performance of the two interpolation methods for the iterative forward projection step. For this simulation, a computer generated noiseless slice, and a phantom slice reconstructed from the Metz filtered projections, were used as the data. The composition of the computer slice is displayed in figure 6.4.

Both slices were forward projected, using either interpolation method, to obtain corresponding sets of projections. Each set of projections was then back-projected, using the same interpolation method as in the forward-projection, to produce a reconstructed slice. The original and reconstructed slices were compared to each other. The robustness of the two interpolation methods was determined by evaluating the ability of each interpolation method to produce projections that reproduced the original image, using the iterative forward projection method, as described in Section 5.3.3. A ψ-comparison index was calculated for each image as a function of the number of iterations.

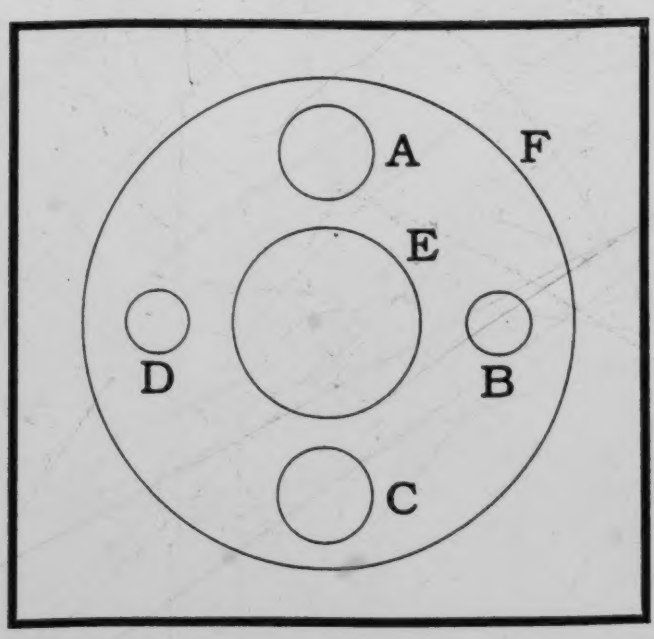

Disc	X-Center	Y-Center	Radius	Magnitude
A	32.5	15	5	50%
B	50	32.5	3	50%
C	32.5	50	5	25%
D	15	32.5	3	75%
E	32.5	32.5	10	100%
F	32.5	32.5	26	10%

Figure 6.4: The computer generated, noiseless slice used for testing the interpolation methods. The magnitude of each disc is a constant and is expressed as the percentage of the maximum pixel count..

Chapter 7

Results

7.1 Takahashi Phantom Results

The improvement indices for Compton window subtraction prior to filtering are plotted as a function of the fraction k, for Metz filtering in figure 7.1, and for Butterworth filtering in figure 7.2. The improvement indices were calculated with respect to the image obtained by filtering the photopeak data set with a Metz filter, constructed from the parameters $P = 1.4$, $S = 30.0$, and $x_m = 4.3$, for the same thickness of scatter material and count level. The optimum k-values for each filtering method and image data, are shown in Table 7.1.

7.2 Jaszczak Phantom Results

To aid in presenting the results for this section, the various parameters for each figure are summarized in Table 7.2.

The improvement indices for the two attenuation correction methods (pre-processing and post-processing) and the two filtering methods (Metz filtering and Compton window subtraction combined with Butterworth filtering) are shown in figure 7.3. The improvement indices were calculated with respect to the slice obtained from the

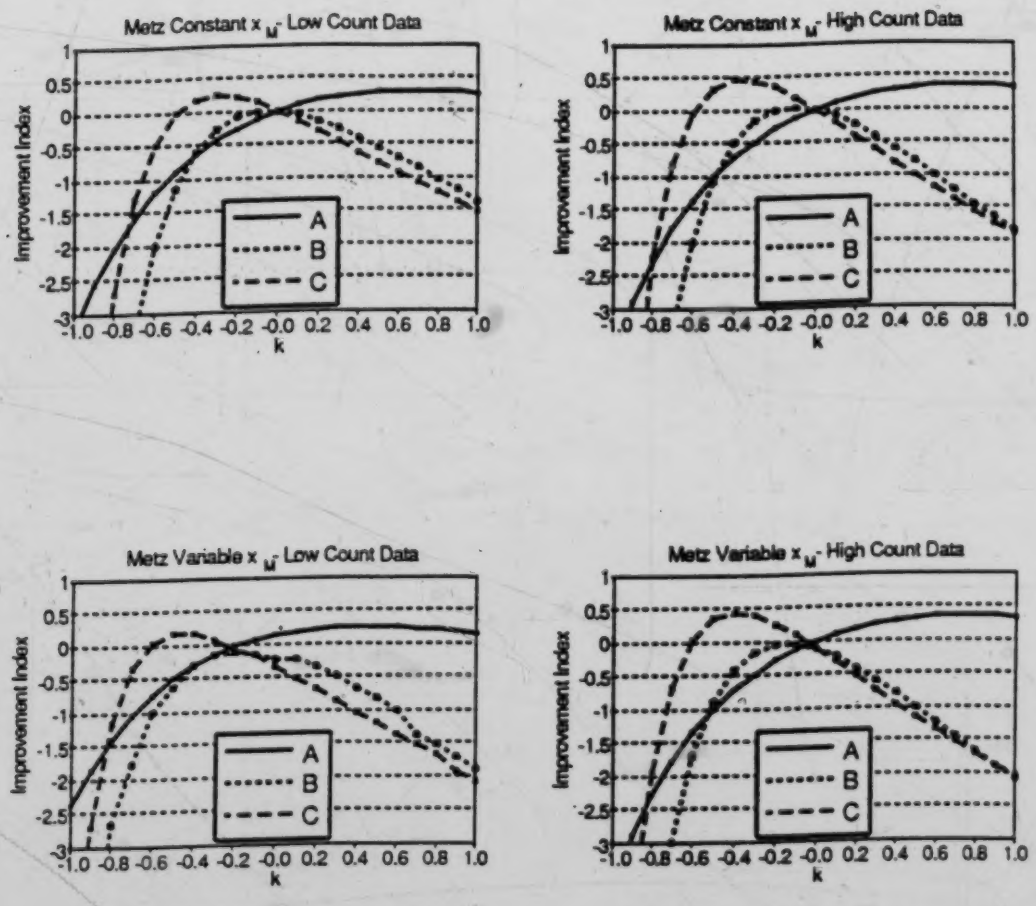
Metz Constant x M - Low Count Data
Metz Constant x M - High Count Data
Metz Variable x M - Low Count Data
Metz Variable x M - High Count Data
Improvement Index
k
A
B
C

Figure 7.1: The improvement indices for Compton window subtraction prior to Metz filtering, as a function of the fraction k, for fixed x_M and variable x_M. Curves A, B, and C correspond to the data for 0.0cm, 5.6cm, and 11.9cm of scatter material respectively.

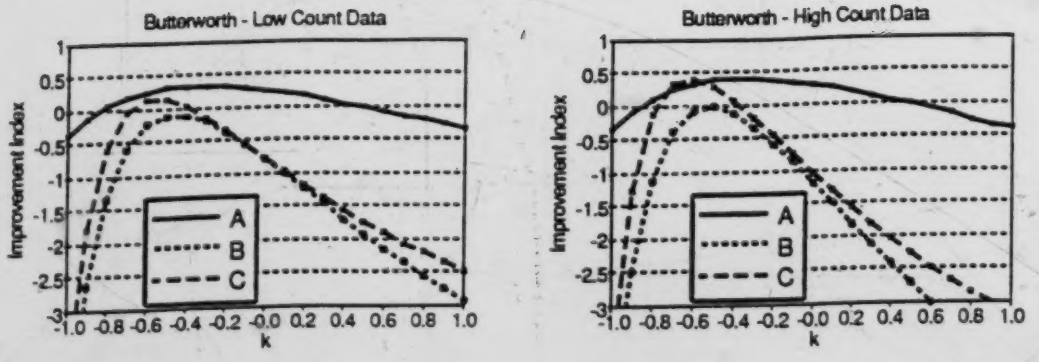

Figure 7.2: The improvement indices for Compton window subtraction prior to Butterworth filtering, as a function of the fraction k. Curves A, B, and C correspond to the data for 0.0cm, 5.6cm, and 11.9cm of scatter material respectively.

Compton Window Subtraction Results						
Data Set	Metz				Butterworth	
	Fixed x_M		Variable x_M			
	k_o	Improvement	k_o	Improvement	k_o	Improvement
Low Count Images						
Image 1	0.7	28%	0.6	20%	-0.4	8%
Image 2	0.0	0%	-0.1	5%	-0.5	37%
Image 3	-0.3	24%	-0.4	32%	-0.6	52%
High Count Images						
Image 4	0.8	34%	1.0	50%	-0.4	15%
Image 5	0.0	0%	-0.1	1%	-0.5	53%
Image 6	-0.4	45%	-0.3	52%	-0.6	71%

Table 7.1: The optimum k-value, k_o, for each set of image data for the three filtering methods. The improvement is the improvement index percentage gained by adding the fraction k_o of the Compton data to the photopeak data prior to filtering, instead of filtering the photopeak data alone with the same filter.

Jaszczak Phantom Figures

Fig #	Plotted	Data	AC	# of Iterations for AC	# of Iterations for FP	Shift	Enlargement	Interpolation Method
7.3	Psi	Both	Both	n/a	n/a	0	0	Linear
7.4	Psi	Metz	Both	n/a	n/a	0	0 to 6	Linear
7.5a	Profile	Metz	Post	n/a	n/a	0	1,3,5	Linear
7.5b	Profile	Metz	Pre	n/a	n/a	0	1,3,5	Linear
7.6	Psi	Metz	Both	n/a	n/a	0,0 to 2,2	0	Linear
7.7a	Profile	Metz	Post	n/a	n/a	0,1 to 0,3	0	Linear
7.7b	Profile	Metz	Pre	n/a	n/a	0,1 to 0,3	0	Linear
7.8a	Psi	Metz	Post	1 to 5	0 to 3	0	0	Linear
7.8b	Psi	Metz	Post	1 to 5	0 to 3	0	0	Area
7.9a	Psi	Metz	Post	1 to 5	0 to 3	0	2	Linear
7.9b	Psi	Metz	Post	1 to 5	0 to 3	0	2	Area
7.10a	Profile	Metz	Post	1 to 3	0	0	1	Linear
7.10b	Profile	Metz	Post	1 to 3	0	0	3	Linear
7.10c	Profile	Metz	Post	1 to 3	0	0	5	Linear
7.11a	Profile	Metz	Post	1 to 3	1	0	1	Linear
7.11b	Profile	Metz	Post	1 to 3	1	0	3	Linear
7.11c	Profile	Metz	Post	1 to 3	1	0	5	Linear
7.12a	Profile	Metz	Post	1 to 3	2	0	1	Linear
7.12b	Profile	Metz	Post	1 to 3	2	0	3	Linear
7.12c	Profile	Metz	Post	1 to 3	2	0	5	Linear
7.13a	Profile	Metz	Post	1 to 3	0	0,1	0	Linear
7.13b	Profile	Metz	Post	1 to 3	0	0,2	0	Linear
7.13c	Profile	Metz	Post	1 to 3	0	0,3	0	Linear
7.14a	Profile	Metz	Post	1 to 3	1	0,1	0	Linear
7.14b	Profile	Metz	Post	1 to 3	1	0,2	0	Linear
7.14c	Profile	Metz	Post	1 to 3	1	0,3	0	Linear
7.15a	Profile	Metz	Post	1 to 3	2	0,1	0	Linear
7.15b	Profile	Metz	Post	1 to 3	2	0,2	0	Linear
7.15c	Profile	Metz	Post	1 to 3	2	0,3	0	Linear

Psi - the ψ comparison or improvement index with the reference image is plotted.
Profile - the profile of the image is plotted.
AC - Attenuation Correction
Pre - Pre-processing attenuation correction method
Post - Post-processing attenuation correction method
FP - Forward Projection

Table 7.2: A summary of the various parameters for each figure in Section 7.2.

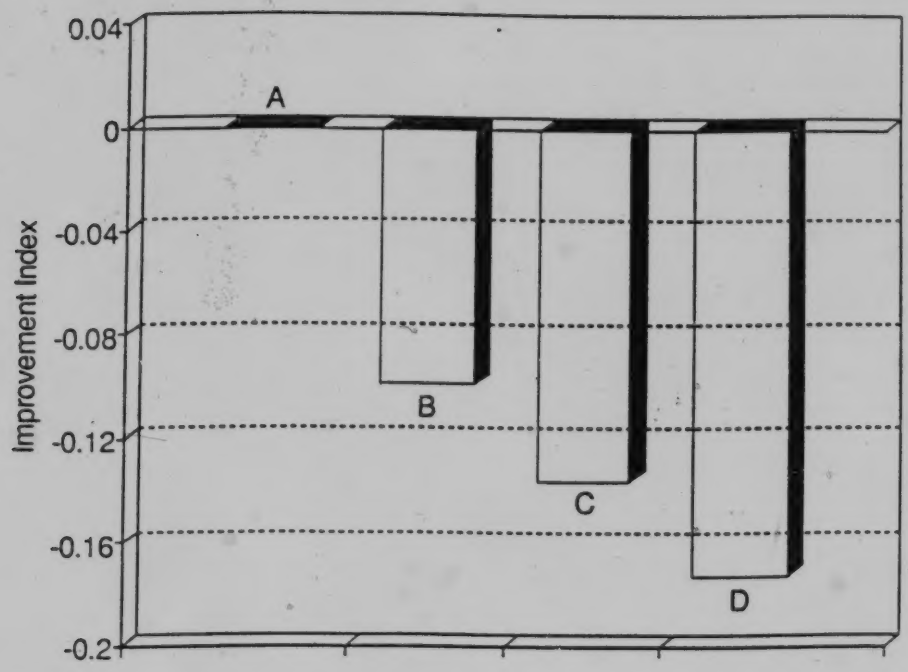

Figure 7.3: The improvement indices for the two attenuation corrections methods and the two filtering methods. Bars **A** and **B** correspond to the slices obtained from the Compton subtracted, Butterworth filtered projections and Metz filtered projections, respectively, using the post-processing attenuation correction method. Bars **C** and **D** correspond to the slices obtained from the Compton subtracted, Butterworth filtered projections and Metz filtered projections, respectively, using the pre-processing attenuation correction method.

Compton subtracted, Butterworth filtered projection data using the post-processing attenuation correction.

The improvement indices for enlarging the boundary for the two attenuation correction methods are shown in figure 7.4. The profiles for the reconstructed images for the exact and for various enlarged boundaries, for the two attenuation correction methods, are shown in figure 7.5.

The improvement indices for shifting the boundary for the two attenuation correction methods are shown in figure 7.6. The profiles for the reconstructed image for the exact and for various shifted boundaries, for the two attenuation correction methods, are shown in figure 7.7.

The results for the iterative post-processing attenuation correction method combined with the iterative forward projection technique using the exact boundary are shown in figure 7.8, for the two interpolation methods. The improvement indices were calculated with respect to the exact boundary case using the non-iterative post-processing attenuation correction method.

The results for the iterative post-processing attenuation method combined with the iterative forward projection technique using a boundary enlarged by 2 pixels are shown in figure 7.9, for the two interpolation methods. The improvement indices were calculated with respect to the exact boundary case using the non-iterative post-processing attenuation correction method.

The profiles for a reconstructed slice, for various numbers of iterations in the

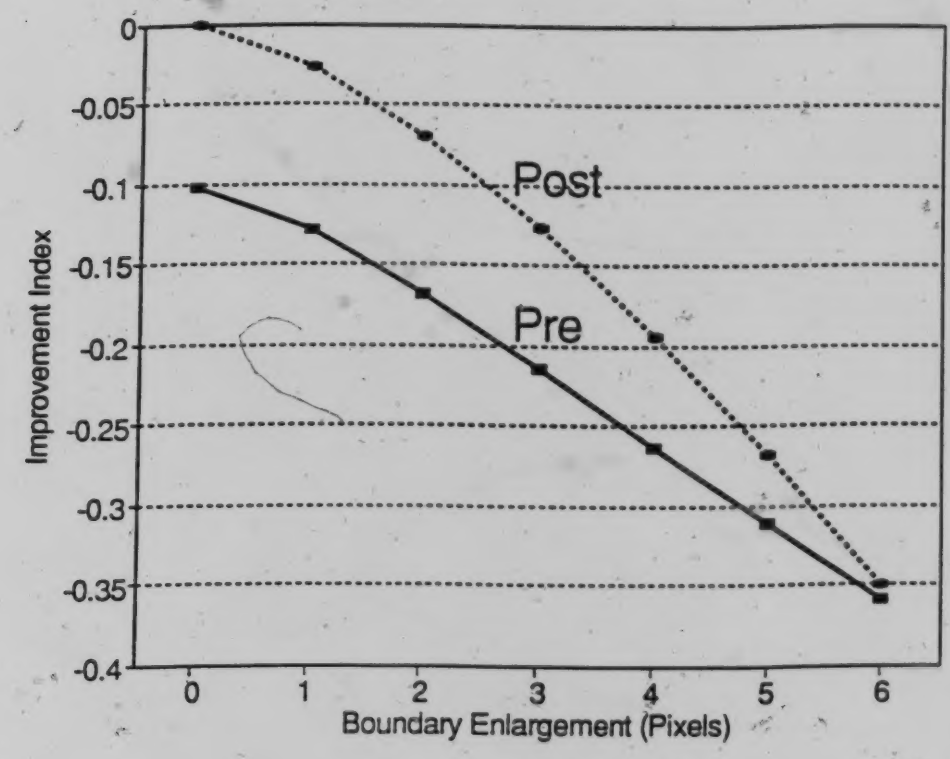

Figure 7.4: The improvement indices, as a function of the enlargement of one of the boundary's axes, for the post-processing and the pre-processing attenuation correction methods. The improvement indices were calculated with respect to the exact boundary case using the post-processing attenuation correction method.

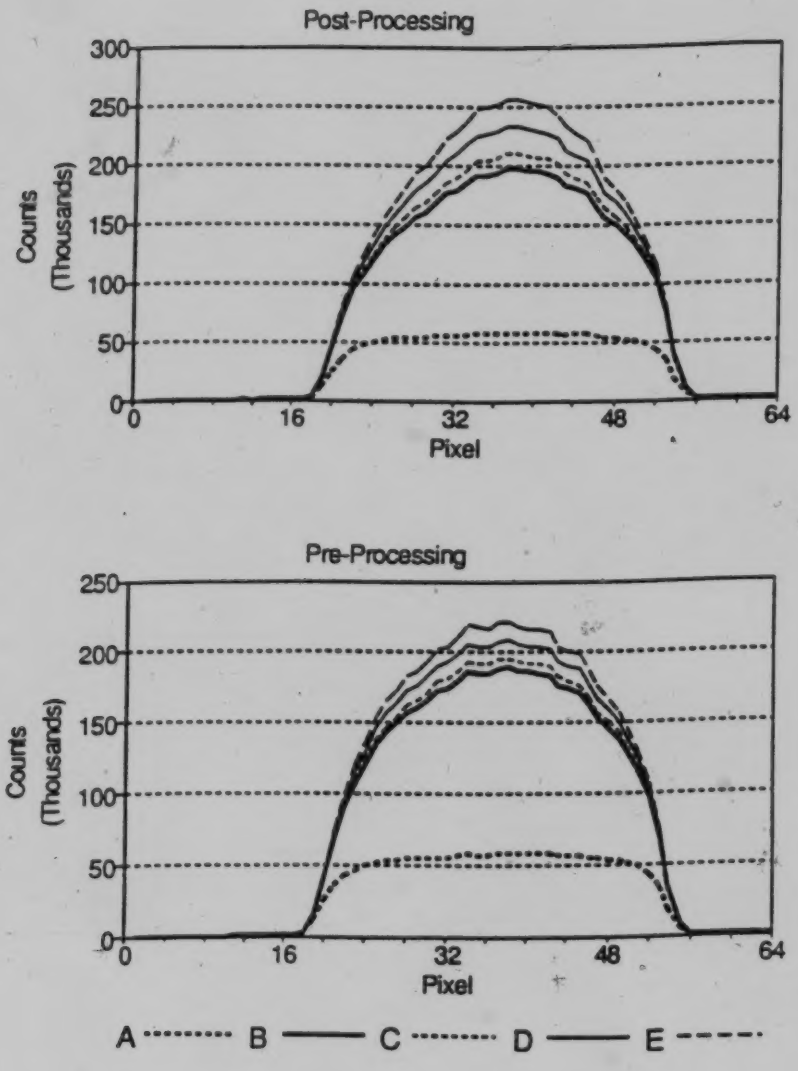

Figure 7.5: The profiles for the reconstructed image for various enlarged boundaries. Curve A is the profile for the reconstructed image without attenuation correction. Curves B, C, D, and E are the profiles for the reconstructed image with attenuation correction using a boundary enlarged by 0, 1, 3, and 5 pixels respectively.

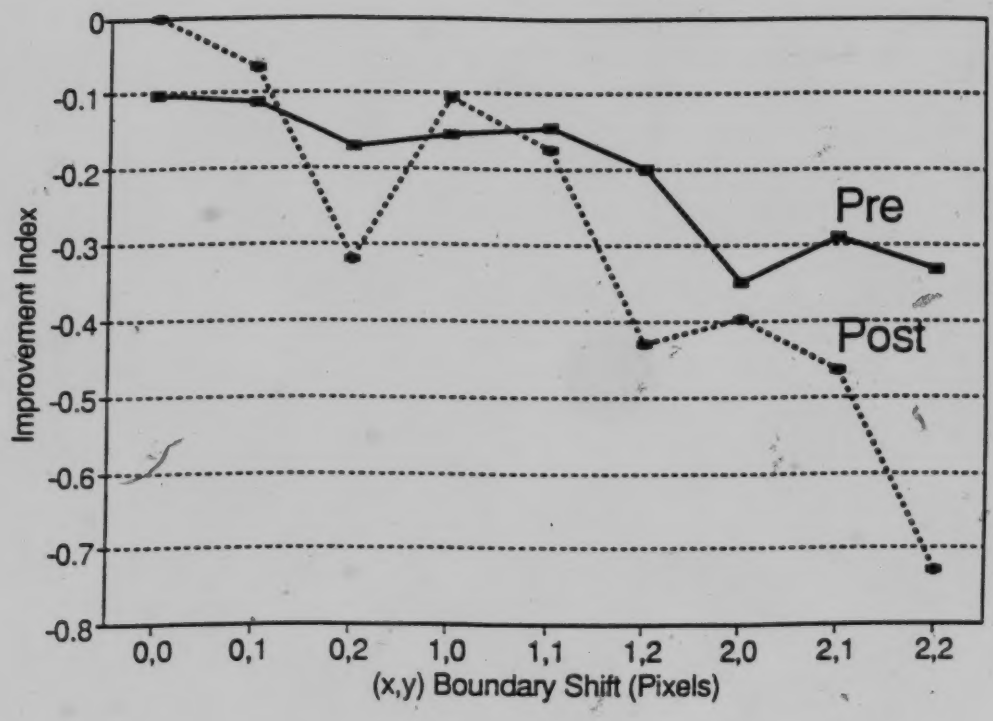

Figure 7.6: The improvement indices, as a function of the shift distance of the boundary, for the post-processing and the pre-processing attenuation correction methods. The improvement indices were calculated with respect to the exact boundary case using the post-processing attenuation correction method.

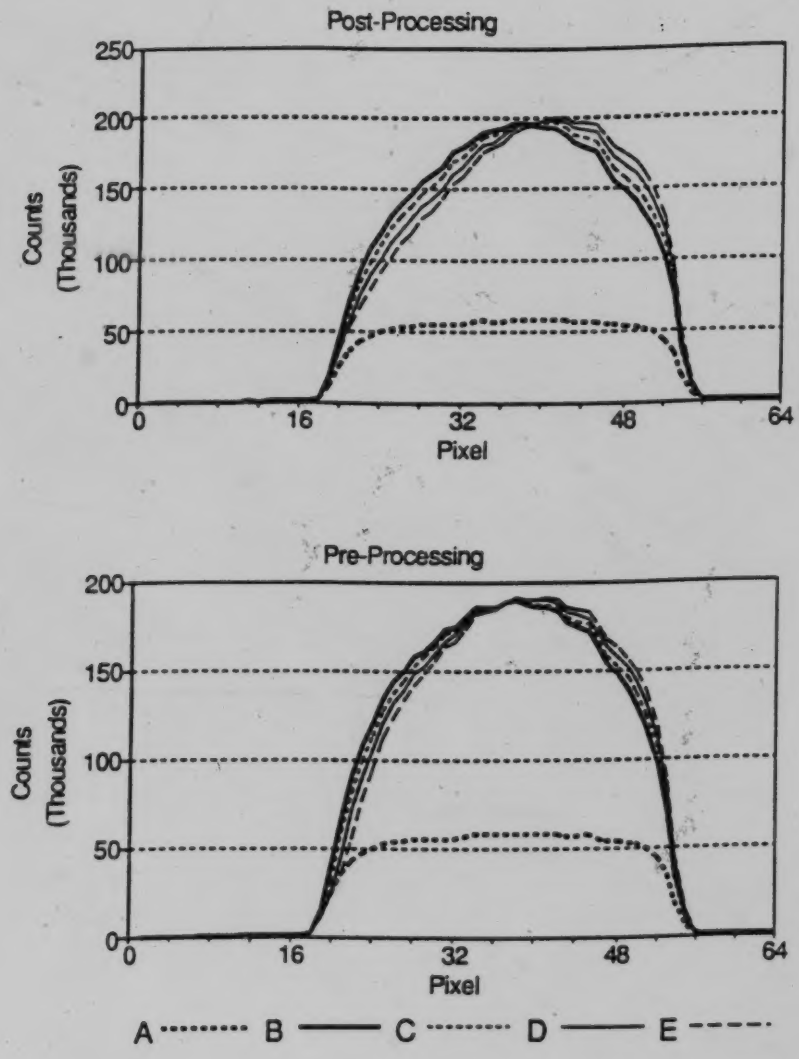

Figure 7.7: The profiles for reconstructed images for various shifted boundaries. Curve A is the profile for the reconstructed image without attenuation correction. Curves B, C, D, and E are the profiles for the reconstructed image with attenuation correction using a boundary shifted by 0, 1, 2, and 3 pixels respectively.

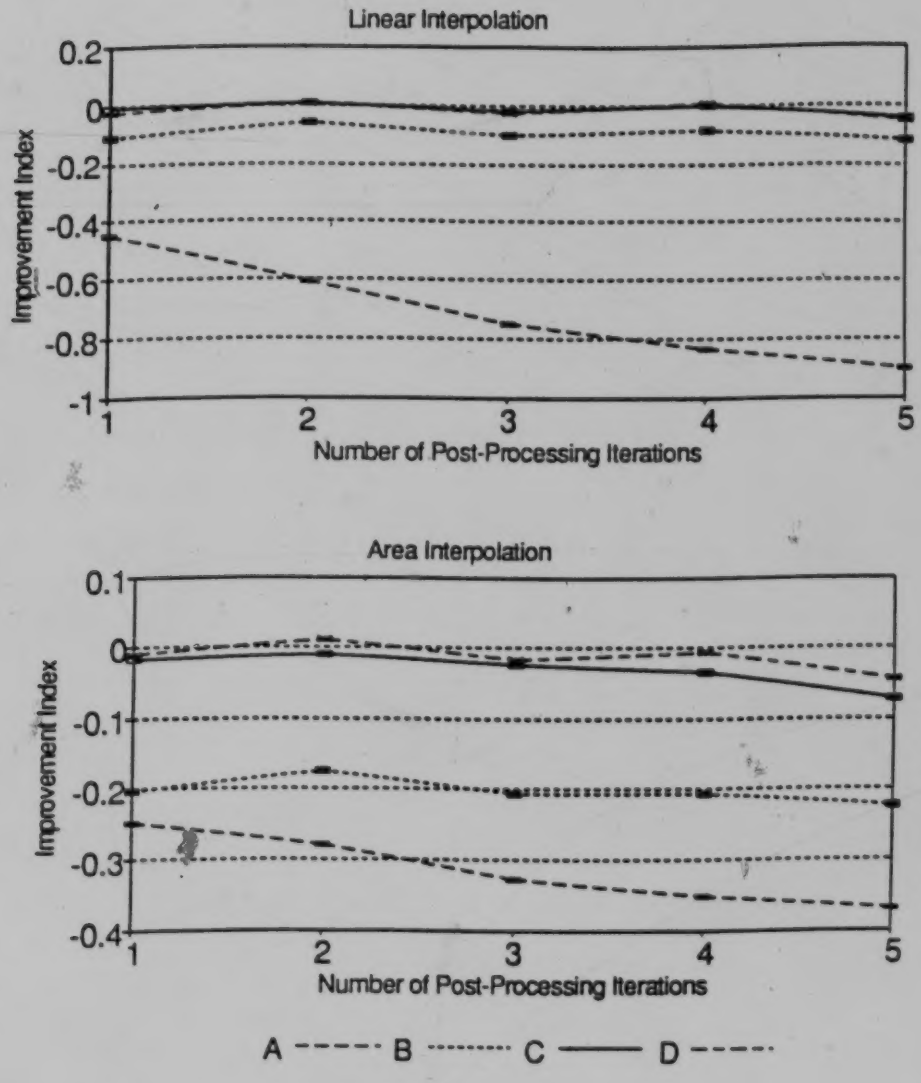

Figure 7.8: The improvement indices, as a function of the number of iterations for the iterative post-processing attenuation correction method combined with the iterative forward projection technique using the exact boundary. Curves A, B, C, and D correspond to 0, 1, 2, and 3 iterations of the iterative forward projection technique, for each iteration of the iterative attenuation correction, respectively.

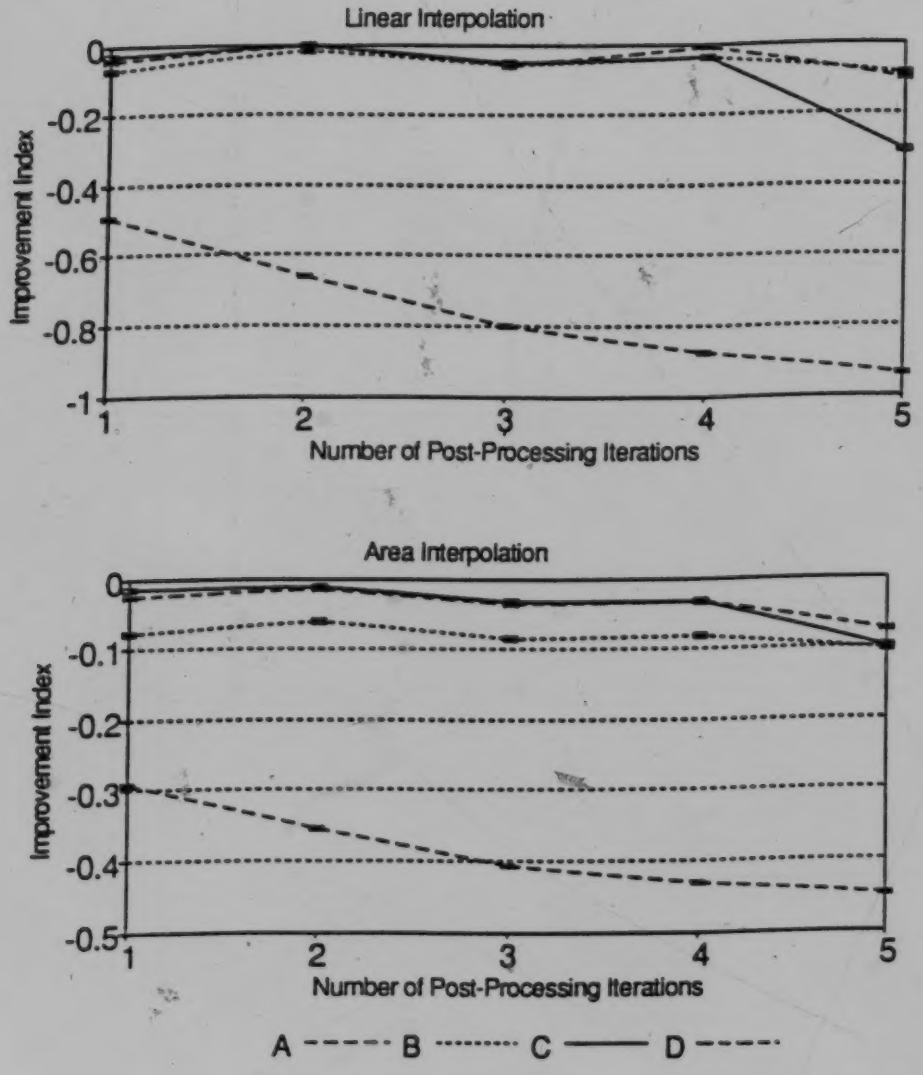

Figure 7.9: The improvement indices, as a function of the number of iterations for the iterative post-processing attenuation correction method combined with the iterative forward projection technique using a boundary enlarged by 2 pixels. Curves A, B, C, and D correspond to 0, 1, 2, and 3 iterations of the iterative forward projection technique, for each iteration of the iterative attenuation correction, respectively.

attenuation correction and forward projection, are shown in figures 7.10 through 7.12 for the enlarged boundaries, and figures 7.13 through 7.15 for the shifted boundaries.

7.3 Computer Simulation Results

The ability of the iterative forward projection technique to reproduce the computer slice and the phantom slice, based on a ψ-comparison, as a function of the number of iterations of the iterative forward projection, for the linear and the area interpolation methods, is shown in figure 7.16.

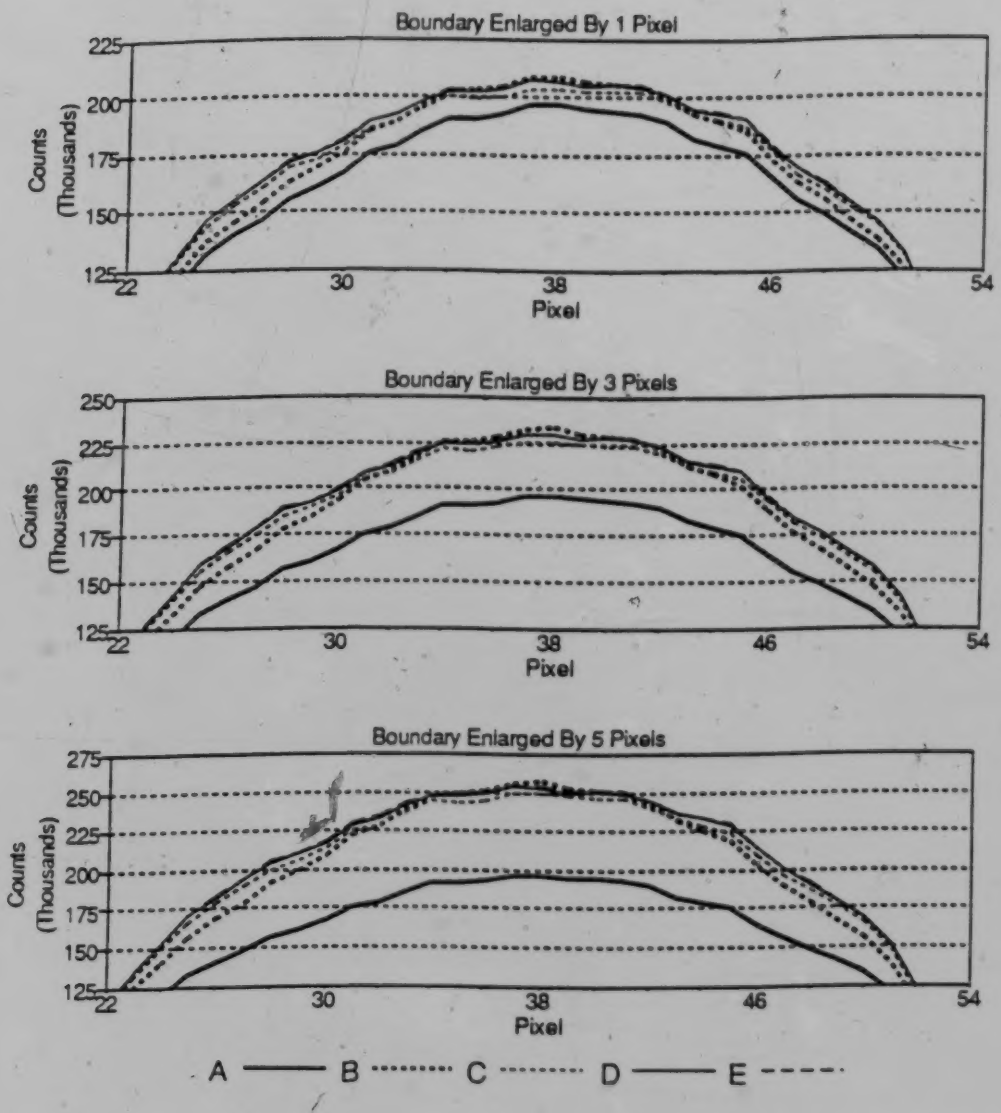

Figure 7.10: The profiles for the reconstructed image using the iterative post-processing attenuation correction method and no iterations in the iterative forward projection for a boundary enlarged by 1 pixel, 3 pixels, and 5 pixels. Curve **A** corresponds to the exact boundary case using the non-iterative post-processing attenuation correction method. Curves **B**, **C**, **D**, and **E** correspond to 0, 1, 2, and 3 iterations of the iterative post-processing attenuation correction using the enlarged boundary.

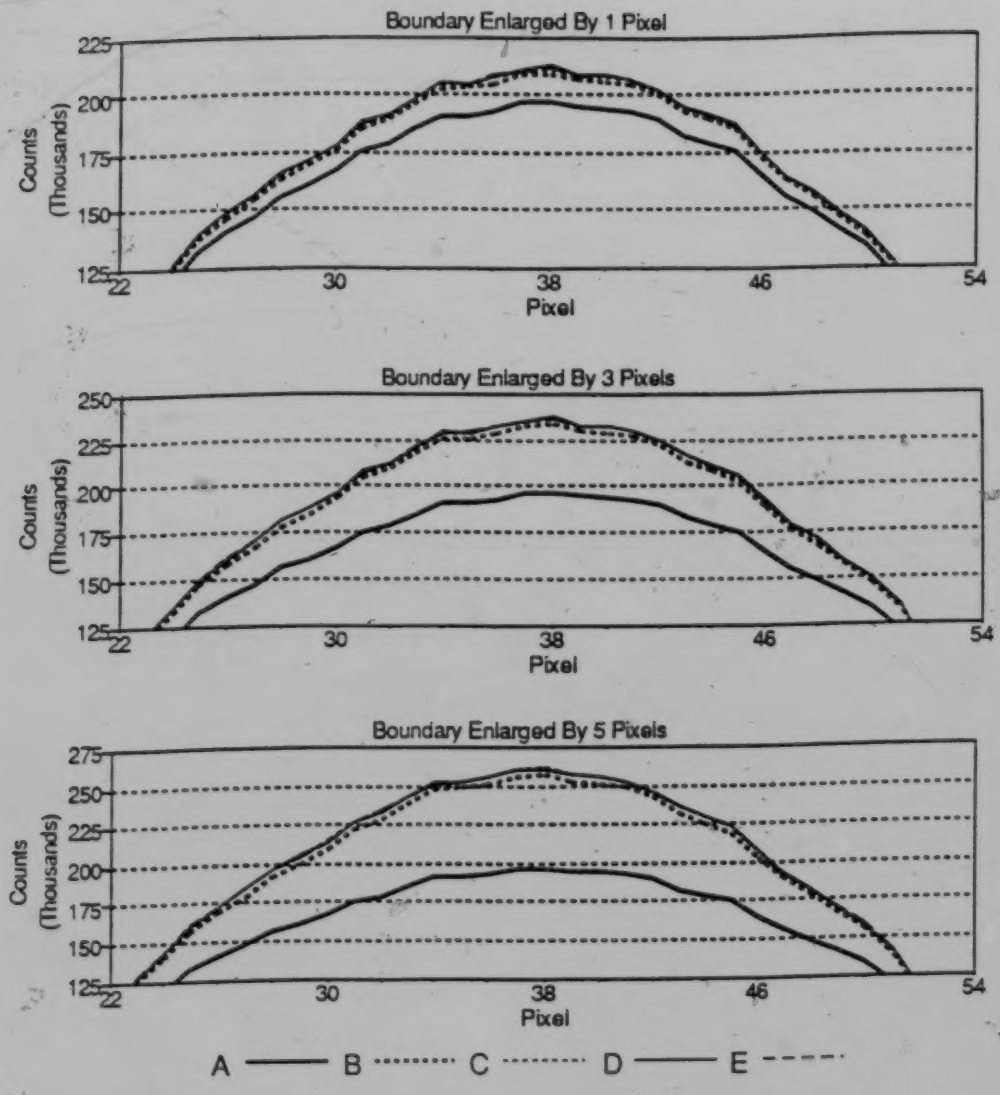

Figure 7.11: Same as figure 7.10 except one iteration of the iterative forward projection technique was performed for each iteration of the iterative post-processing attenuation correction.

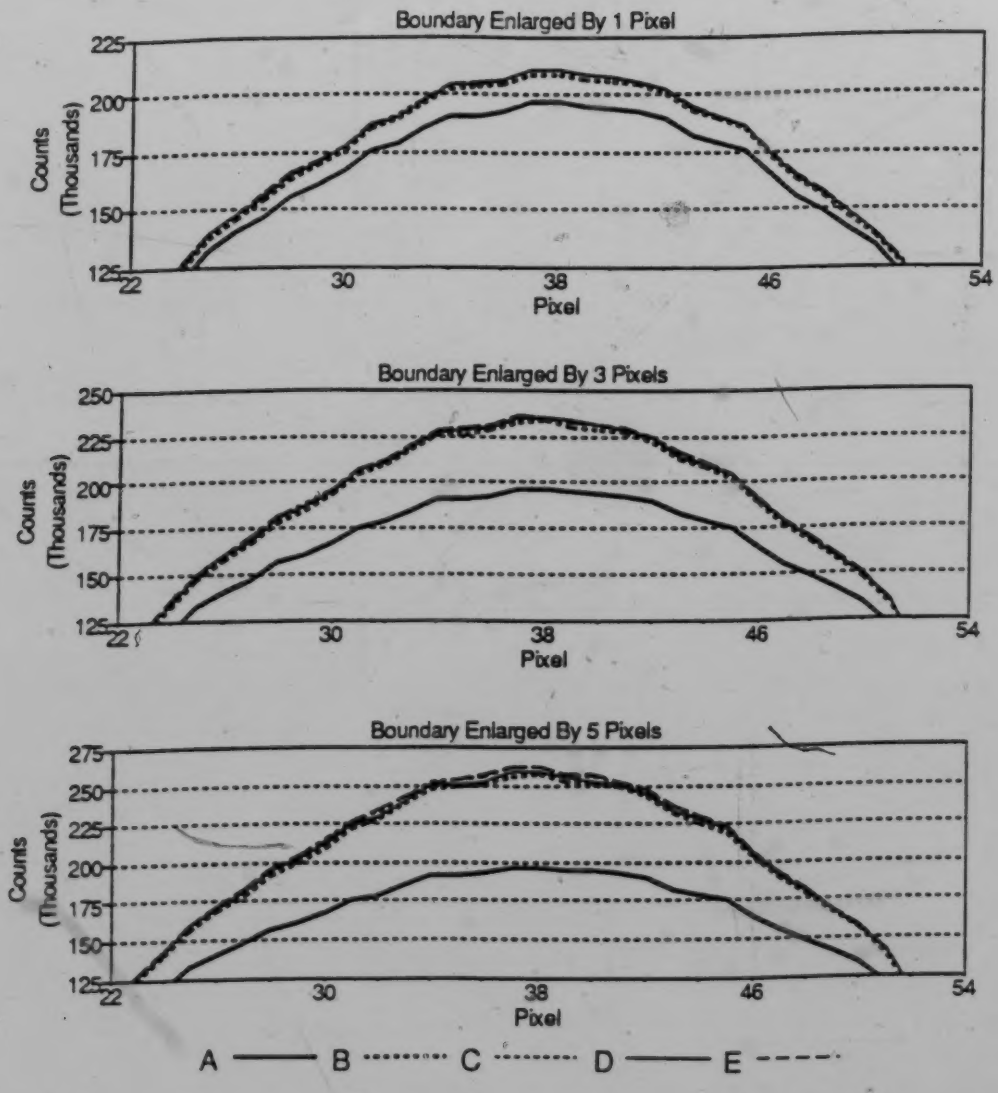

Figure 7.12: Same as figure 7.10 except two iterations of the iterative forward projection techniques were performed for each iteration of the iterative post-processing attenuation correction.

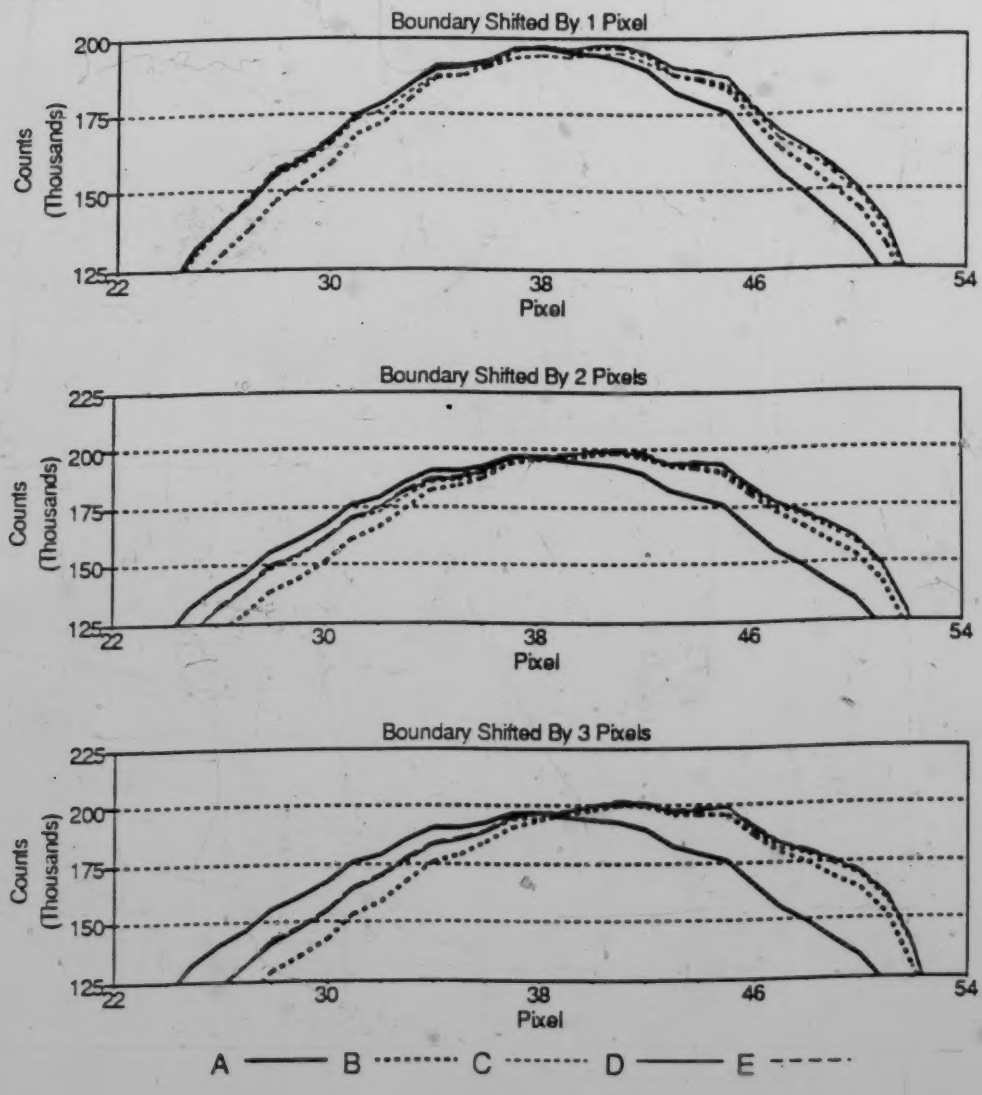

Figure 7.13: The profiles for the reconstructed image using the iterative post-processing attenuation correction method and no iterations of the iterative forward projection technique for a boundary shifted by 1 pixel, 2 pixels, and 3 pixels. Curve A corresponds to the exact boundary case using the non-iterative post-processing attenuation correction method. Curves B, C, D, and E correspond to 0, 1, 2, and 3 iterations of the iterative post-processing attenuation correction using the shifted boundary.

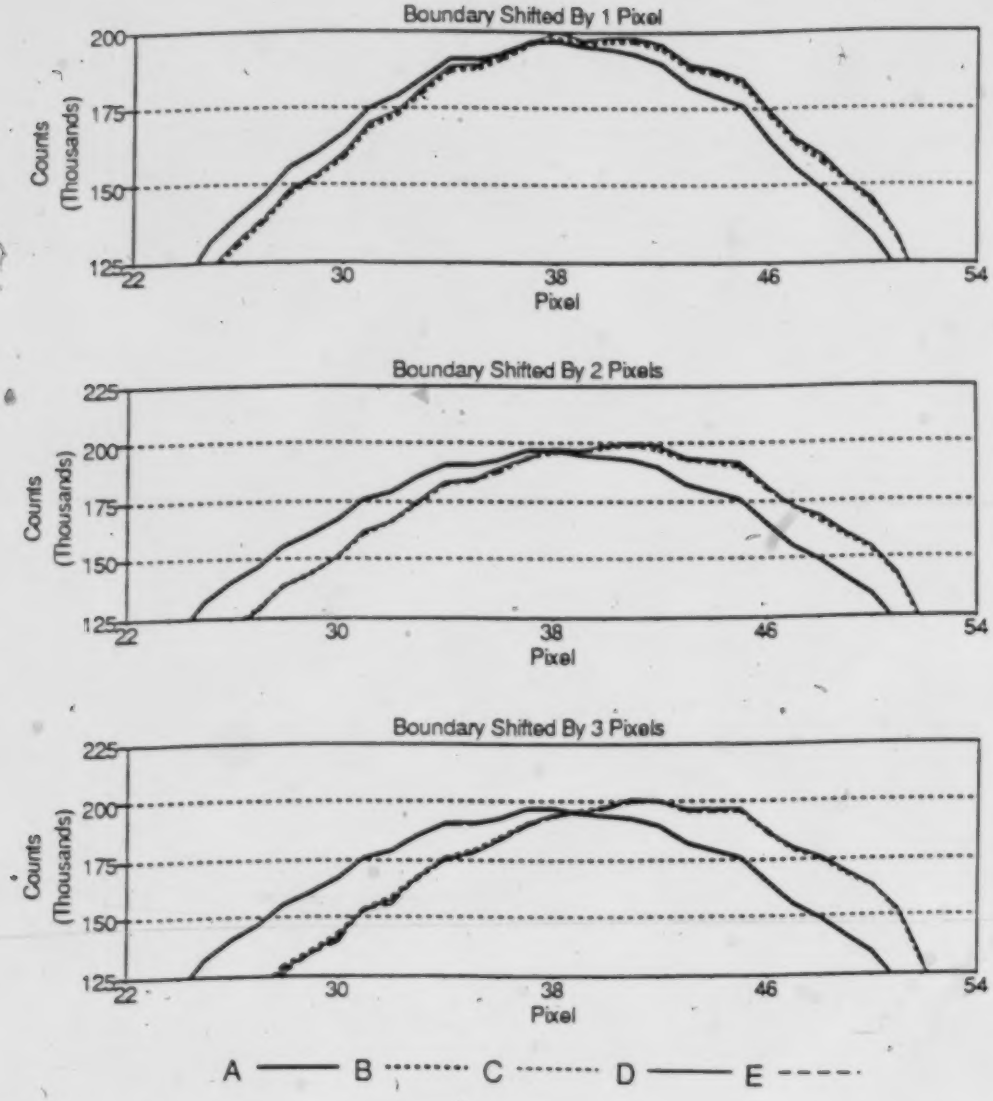

Figure 7.14: Same as figure 7.13 except one iteration of the iterative forward projection technique was performed for each iteration of the iterative post-processing attenuation correction.

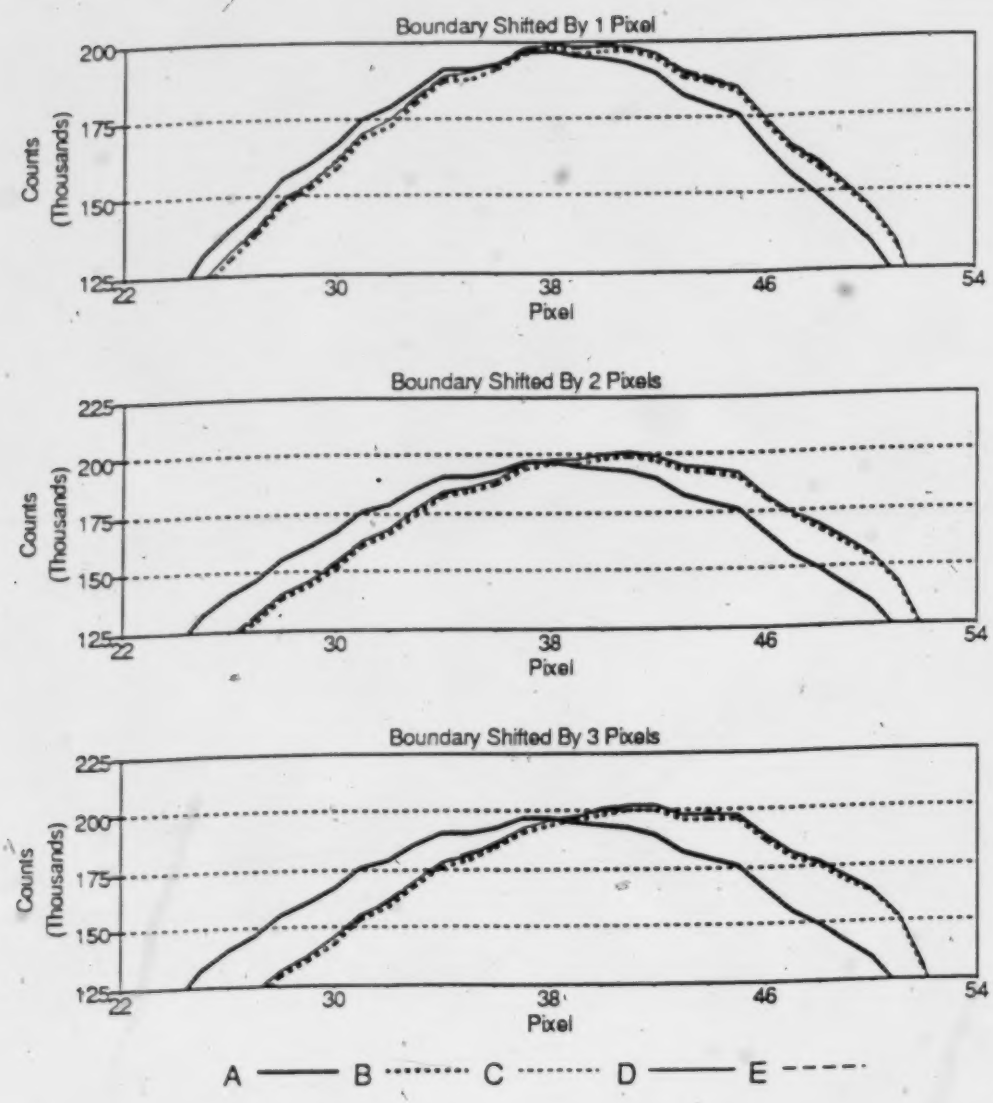

Figure 7.15: Same as figure 7.13 except two iterations of the iterative forward projection techniques were performed for each iteration of the iterative post-processing attenuation correction.

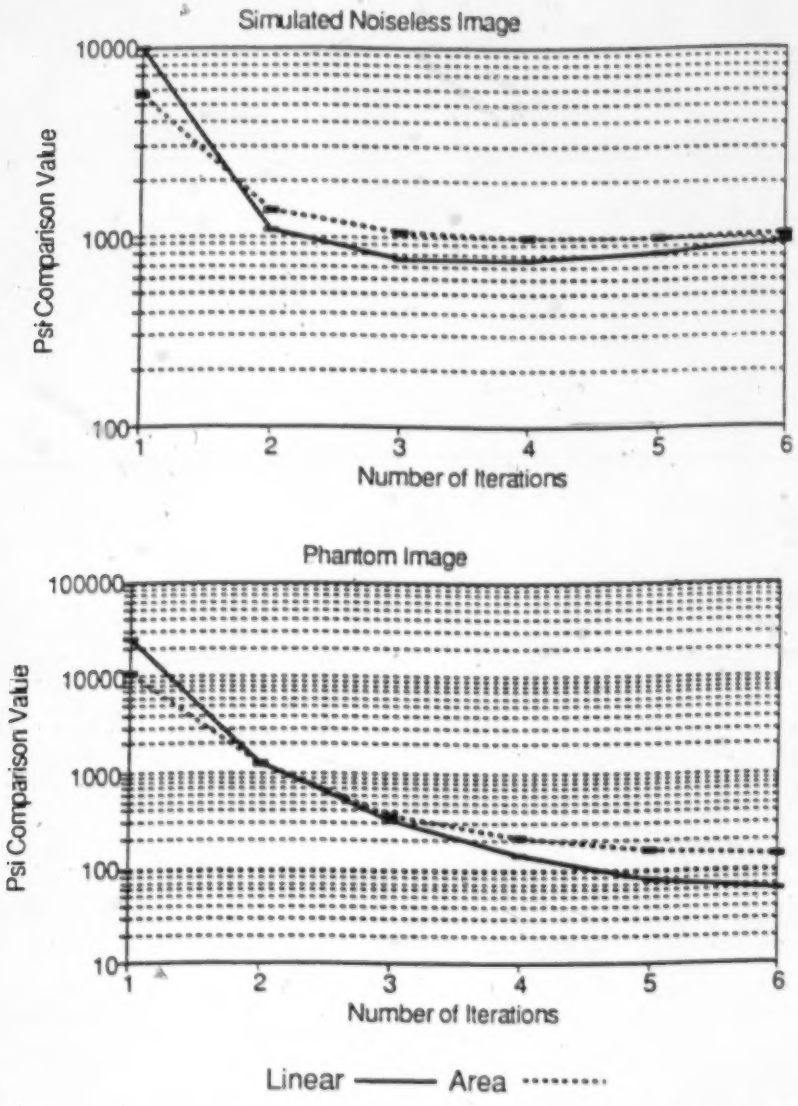

Figure 7.16: The convergence of reproduced images to the original image, based on the ψ-comparison index, as a function of the number of iterations of iterative forward projection. The ψ-comparison was calculated using the original slice as the reference image.

Chapter 8

Discussion of Results

8.1 Takahashi Phantom Results

The purpose of this experiment was to determine if subtracting a portion of the Compton window data from the photopeak window data prior to filtering would provide any improvement over filtering the photopeak data alone. Secondly, if an improvement can be obtained from the Compton window subtraction technique, was the method robust for different thicknesses of scatter material. The filters used in this experiment are constructed from values known to perform robustly in the typical SPECT imaging situation [Ta89]. The Metz filter parameters P=1.4 and S=30.0 accurately model the MTF of the system for 5.0 cm of scatter material and a source to collimator distance of 10 cm using technetium 99m.

The results of subtracting the Compton window data from the photopeak window data are shown in figures 7.1 and 7.2, and the optimum values of k are displayed in Table 7.1. These results demonstrated that Compton window subtraction, prior to Butterworth or Metz filtering, can improve the images. For Butterworth filtering, a single value of k was optimum and provided significant improvements for all thicknesses of scatter material investigated. The optimum value of k for Metz filtering,

for both a constant x_M and an image dependent x_M, was quite dependent upon the thickness of scatter material present, and to a lesser extent the count level (and hence the noise) of the images.

The Compton window subtraction technique should be used in conjunction with Butterworth filtering. It was found that a value of $k \approx -0.5$ was sufficient for all thicknesses of scatter material investigated. The combination of Compton window subtraction and Butterworth filtering reduced both the scatter component and the noise in the image, and hence, a significant improvement was gained over filtering the photopeak data alone with a Butterworth filter.

The Compton window subtraction technique should not be used in conjunction with Metz filtering since it was not robust due to k's dependence upon the amount of scatter material present. The Metz filter used was dependent upon the MTF of the system, which included a scatter component, and was capable of partially removing the effects of scatter photons in an image. Therefore, the use of Compton window subtraction was somewhat redundant when using Metz filtering and would likely degrade the images, since the thickness of scatter material will not be a constant for typical projection images. Using either a constant x_M or an image dependent x_M, for the Metz filter, had no significant consequences on the outcome of the images.

The subtraction of Compton data from the photopeak data removes a broad background from the photopeak image. Thus, although contrast in the image may be enhanced, the relative noise per pixel will certainly increase since the average

pixel count will decrease. The addition of the Compton data to the photopeak data has the inverse effects; contrast may decrease, but the noise per pixel will also decrease since the average pixel count will increase. These factors may explain why, in figures 7.1 and 7.2, the improvement index drops off more quickly in the negative k-direction than in the positive k-direction.

8.2 Jaszczak Phantom Results

The purpose of this experiment was, firstly, to evaluate the performance of two attenuation correction techniques relative to one another. Secondly, and more clinically relevant, was the effect of distorting or mispositioning the attenuation boundary on the two attenuation correction techniques. Lastly, extra iterations of the post-processing attenuation correction technique were investigated to determine if the extra iterations improve the image for the exact boundary, or correct for either distortioning or mispositioning the boundary.

The linear attenuation coefficient μ, used for the attenuation correction techniques, was given the value $\mu = 0.14$ cm^{-1} to compensate for the broad beam geometry of the imaging situation. This was done since the scatter reduction methods used in this work (i.e. Metz filtering and Compton window subtraction) only partially compensate for the in-scatter component, in the projections. Empirically, by comparing reconstructed slices with the reference slice, it was determined that the value $\mu = 0.14$ cm^{-1} provided the best ψ-comparison index, for both the pre-

processing and the post-processing attenuation correction methods, for both sets of filtered projections. This value for the attenuation coefficient produced reconstructed slices that were very uniform in count density, with neither a dip nor a peak in the density of counts within the central region of the slice.

The distance between the phantom and the collimator was kept to a minimum, at each projection angle, by using an elliptical orbit. Keeping the phantom-to-collimator distance to a minimum minimized the loss of resolution that occurs as the source-to-collimator distance increases. An elliptical orbit was required since the diameter of phantom was less than the width of the patient bed.

Both the pre-processing and the non-iterative post-processing attenuation correction methods greatly improved the ψ-comparison index to the reference image, for the exact boundary. Figure 7.3 demonstrates that the non-iterative post-processing technique is slightly better than the pre-processing method. Figure 7.8 illustrates that, for the exact boundary case, adding post-processing iterations without including forward projection iterations produces a less accurate image than obtained with no iterations. Including forward iterations with each post-processing iteration improves the accuracy, but the results are still not significantly better than for the non-iterative method.

In a clinical setting the boundary cannot always be accurately defined. Figures 7.4 through 7.7 suggest that, although the pre-processing attenuation correction method is less accurate than non-iterative post-processing, it is also less sensitive

to boundary shifts and enlargements and hence more robust. A similar result was reported by Marcey *et al.* for the sensitivity of the attenuation correction methods for boundary enlargements [Ma88]. Figure 7.9 confirms that adding post-processing iterations without including forward projection iterations produces less accurate images, but also demonstrates that with an appropriate number of forward projection and post-processing iterations, this technique can correct for boundary enlargements. The technique is not robust, however, since the results are sensitive to the number of forward projection and post-processing iterations used and do not converge as the number of iterations increase. These results for boundary enlargement are confirmed in the profiles displayed in figures 7.10 through 7.12. Figures 7.13 through 7.15 show that boundary shifts produce significant asymmetries in the images, which are not removed by the iterative techniques. The asymmetries produced by the post-processing attenuation correction method for shifted boundaries have also been reported by Hosoba *et al.* [Ho86].

It should be noted that the results obtained from this experiment may be quite different for a hot-spot phantom than for the cold-spot phantom used in this work. Also, both the non-iterative and the iterative forward projection techniques used were based on parallel forward and backward projection, and not the geometric response function of the system. As such these methods do not accurately mimic the true physical situation.

8.3 Computer Simulation Results

Figure 7.16 demonstrates that, if an image is forward projected and then the projections are backprojected, the resulting image differs from the original. This is illustrated both for a noiseless (simulated) image, and for a typical phantom image, using either linear or area interpolation. With only a single iteration, area interpolation is better than linear interpolation. If additional iterations are used, the comparison between the final and original image improves significantly, and linear interpolation provides better results than area interpolation. These findings confirm the results shown in figures 7.8 and 7.9.

It is interesting to note that both interpolation methods continue to converge for up to 6 iterations for the phantom image (figure 7.16b), but diverges after two iterations for linear interpolation, and four iterations for area interpolation, for the simulated image (figure 7.16a). The forward and backward projection iterations cannot reproduce the original images, even after iterations, due to the discrete nature of the problem, and therefore it is not surprising that the convergence is limited for the noiseless slice.

Chapter 9

Conclusion

Scatter reduction and attenuation correction methods were evaluated, for the traditional filtered backprojection method of reconstruction used in SPECT imaging. Two sets of experiments were performed. The first set of experiments was used to study the reduction of scatter in planar projection images, prior to reconstruction, using Compton window subtraction in conjunction with digital image filtering techniques. The second set of experiments was used to study attenuation correction methods applicable to the traditional filtered backprojection method of reconstruction.

The first set of experiments demonstrates that both Metz filtering, and Compton window subtraction prior to Butterworth filtering, reduce the scatter component present in typical SPECT images. Compton window subtraction should be used prior to Butterworth filtering since image quality improves and the fraction of the Compton window data subtracted is relatively constant for a wide range of scatter material thicknesses. However, Compton window subtraction should not be used prior to Metz filtering both because the improvement in image quality is at best small, and the optimum fraction of the Compton window data subtracted varies significantly with the thickness of scatter material.

The second set of experiments shows that both the pre-processing and non-iterative post-processing attenuation correction methods improve the quantitative accuracy of reconstructed SPECT images provided the boundary is correctly defined. Iterative post-processing attenuation correction reduces the accuracy of the reconstructions compared to the non-iterative method. When the boundary is enlarged, the iterative techniques can improve reconstruction accuracy, but if the boundary is mispositioned, iterative techniques cannot remove the asymmetries introduced by the boundary shift.

A computer simulation was used to examine two interpolation methods. In general, linear interpolation was superior to area interpolation.

9.1 Suggestions for Future Work

In this work it was shown that modifications to the traditional filtered backprojection method of reconstruction, involving corrections for scatter and attenuation, can improve both the qualitative appearance and the quantitative accuracy of the reconstructed images. These methods help to some extent but are limited (i.e. not robust) and would be difficult to apply to general clinical imaging situations. These methods were derived through approximations and assumptions, and strictly compensate for the effects of scatter and attenuation. In future work, more sophisticated methods of reconstruction should be investigated that account for the processes responsible for scatter and attenuation, and incorporate much of the a priori knowledge

of the imaging situation.

Bibliography

[Ah89] Ahluwalia BD. *Tomographic Methods in Nuclear Medicine: Physical Principles, Instrumentation, and Clinical Applications.* Boca Raton, Florida: CRC Press, Inc., 1989:3-34

[An84] Anger RT. The Anger Scintillation Camera - A Review. In *Physics in Nuclear Medicine - Recent Advances.* Rao DV, Chandra R, Graham MC (eds.), American Institute of Physics, New York, 1984: 32-55

[Bu79] Budinger TF, Gullberg GT, Huesman RH. Emission Computed Tomography. In *Image Reconstruction from Projections – Implementation and Applications.* Herman GT (ed.), Springer-Verlag, New York, 1979: 211-216

[Ch78] Chang L-T. A method for attenuation correction in radionuclide computed tomography. *IEEE Transactions on Nuclear Science*, 1978; 1:638-643

[Cr86] Croft BY. *Single-Photon Emission Computed Tomography.* Chicago: Year Book Medical Publishers, Inc., 1986:1-164

[De89] DeVito RP, Hamill JJ, Treffert JD, Stoub EW. Energy-weighted acquisition of scintigraphic images using finite spatial filters. *Journal of Nuclear Medicine*, 1989; 12:2029-2035

[Fl84] Floyd CE, Jaszczak RJ, Harris CC, Coleman RE. Energy and spatial distribution of multiple order compton scatter in SPECT: a Monte Carlo investigation. *Physics of Medicine and Biology*, 1984; 10:1217-1230

[Fl88] Floyd CE, Jaszczak RJ, Coleman RE. Scatter detection in SPECT imaging: dependence on source depth, energy, and energy window. *Physics of Medicine and Biology*, 1988; 9:1075-1081

[Gu81] Gullberg GT, Budinger TF. The use of filtering methods to compensate for constant attenuation in single-photon emission computed tomography. *IEEE Transactions on Biomedical Engineering*, 1981; 28:142-157

[Ha89] Hamill JJ, DeVito RP. Scatter reduction with energy-weighted acquisition. *IEEE Transactions on Nuclear Science*, 1989; 2:1334-1339

[He80] Herman GT. *Image Reconstruction from Projections - The Fundamentals of Computerized Tomography.* New York: Academic Press, Inc., 1980:90-117

[Ho86] Hosoba M, Wani H, Toyama H, Murata H, Tanaka E. Automated body contour detection in SPECT: effects on quantitative studies. *The Journal of Nuclear Medicine*, 1986; 27:1184-1191

[Ka88a] Kak AC, Slaney M. *Principles of Computerized Tomographic Imaging.* New York: IEEE Press., 1988:49-75

[Ka88b] Kak AC, Slaney M. *Principles of Computerized Tomographic Imaging*. New York: IEEE Press., 1988:135-142

[Ki84] King MA, Doherty PW, Schwinger RS. Digital Image Filtering of Nuclear Medicine Images. In *Physics in Nuclear Medicine - Recent Advances*. Rao DV, Chandra R, Graham MC (eds.), American Institute of Physics, New York, 1984: 310-331

[Ki87] King MA, Glick SJ, Penney BC, Schwinger RB, Doherty PW. Interactive visual optimization of SPECT preconstruction filtering. *Journal of Nuclear Medicine*, 1987; 7:1192-1198

[Ko90] Koral KF, Swailem FM, Buchbinder S, Clinthorne NH, Rogers WL, Tsui BMW. Spect dual-energy-window compton correction: scatter multiplier required for quantification. *Journal of Nuclear Medicine*, 1990; 1:90-98

[Ma88] Macey DJ, DeNardo GL, DeNardo SJ. Comparison of three boundary detection methods for SPECT using Compton scattered photons. *Journal of Nuclear Medicine*, 1988; 29:203-207

[Si87] Singh M, Horne C. Use of germanium detector to optimize scatter correction in SPECT. *Journal of Nuclear Medicine*, 1987; 12:1853-1860

[Ta89] Takahashi A. *Evaluation of Filters for Single Photon Emission Computed Tomography*, MSc Thesis, Department of Physics, University of Alberta, Edmonton, 1989